

Gö-VIP 36: Prof. Dr. Emilie Macé, Klinik für Augenheilkunde

Visual objects refine head direction coding

Science, September 2025, 389(6765), <https://doi.org/10.1126/science.adu9828>

Dominique Siegenthaler^{1,2,3,4}, Henry Denny⁴, Sofía Skromne Carrasco⁴, Johanna Luise Mayer^{1,2,3}, Daniel Levenstein^{4,5}, Adrien Peyrache^{4,*}, Stuart Trenholm^{4,*}, Emilie Macé^{1,2,3,*}

¹ Brain-Wide Networks Group, Department of Ophthalmology, University Medical Center Göttingen, Else Kröner Fresenius Center for Optogenetic Therapies, Göttingen, Germany.

² Cluster of Excellence "Multiscale Bioimaging: From Molecular Machines to Networks of Excitable Cells" (MBExC), University of Göttingen, Germany.

³ Brain-Wide Circuits for Behavior Research Group, Max Planck Institute for Biological Intelligence, Planegg, Germany.

⁴ Montreal Neurological Institute, McGill University, Montreal, QC, Canada.

⁵ Mila, Montreal, QC, Canada.

* Corresponding Author

Summary (ENG)

In our day-to-day life, we use visual objects (e.g., a specific clock tower when walking around town, etc.) as spatial landmarks to help orientate ourselves as we make our way through the world. The visual world is parsed into objects while our location in the world is processed by specialized cells such as place cells, grid cells, and head direction cells in the brain's spatial navigation system. However, much remains unknown about how visual objects modulate the activity of spatial navigation neurons, partly because it is unclear how visual objects are processed in the rodent brain, where spatial navigation signals have been most extensively studied.

To address this gap in knowledge, we reasoned that a brainwide activity screen in mice could identify visual object–preferring areas in an unbiased way. Our brainwide screen based on functional ultrasound imaging revealed that spatial navigation–related areas, not visual cortical areas, tended to show a preference for visual objects. The postsubiculum, a hub of the head direction system, exhibited the strongest object preference. Using electrophysiology, we discovered that head direction cells were differentially modulated by a visual object based on their preferred firing direction. Viewing the object increased the response of head direction cells that code toward the object while simultaneously decreasing the firing rate of head direction cells that code directions away from the object.

As an analogy, imagine yourself wandering around a city with a compass (which, in our experiments, is the brain's head direction system), and each time you look at a landmark (which, in our experiments, is an image of an object), the compass needle becomes more stable and thus more accurate. Together, these results provide insights into how the brain uses visual landmarks to dynamically enhance the encoding of spatial information about the world.

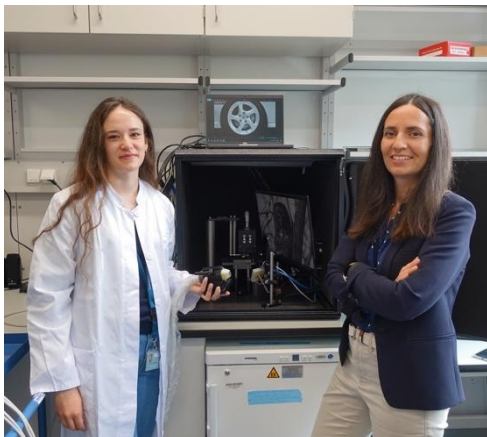
Zusammenfassung (DE)

In unserem Alltag nutzen wir visuelle Objekte (z. B. einen bestimmten Kirchturm beim Gehen durch die Stadt) als räumliche Referenzpunkte, um uns bei der Orientierung in unserer Umgebung besser zurechtzufinden. Die visuelle Welt wird dabei in Objekte zerlegt, während unsere Position in der Welt durch spezialisierte Zellen im räumlichen Navigationssystem des Gehirns verarbeitet wird, etwa durch Ortszellen, Gitterzellen und Kopfrichtungszellen. Dennoch ist bislang wenig darüber bekannt, wie visuelle Objekte die Aktivität von Neuronen des räumlichen Navigationssystems modulieren. Ein Grund hierfür ist, dass unklar ist, wie

visuelle Objekte im Nagetiergehirn verarbeitet werden – dem Modellsystem, in dem räumliche Navigationssignale bislang am umfassendsten untersucht wurden.

Um diese Wissenslücke zu schließen, gingen wir davon aus, dass ein gehirnweiter Aktivitätsscreen in Mäusen auf unvoreingenommene Weise Areale identifizieren könnte, die visuelle Objekte bevorzugen.. Unser auf funktioneller Ultraschallbildgebung basierender gehirnweiter Screen ergab, dass nicht visuelle kortikale Areale, sondern vielmehr Areale, die mit räumlicher Navigation in Verbindung stehen, eine Präferenz für visuelle Objekte aufwiesen. Das Postsubiculum, ein Zentrum des Kopfrichtungssystems, zeigte dabei die stärkste Objektpräferenz. Mithilfe elektrophysiologischer Messungen konnten wir nachweisen, dass Kopfrichtungszellen durch ein visuelles Objekt in Abhängigkeit von ihrer bevorzugten Feuerrichtung unterschiedlich moduliert werden. Das Betrachten des Objekts erhöhte die Aktivität jener Kopfrichtungszellen, die in Richtung des Objekts kodieren, während gleichzeitig die Feuerrate von Kopfrichtungszellen abnahm, die Richtungen weg vom Objekt kodieren.

Als Analogie kann man sich vorstellen, dass man sich mit einem Kompass (der in unseren Experimenten dem Kopfrichtungssystem des Gehirns entspricht) durch eine Stadt bewegt, und jedes Mal, wenn man einen Orientierungspunkt betrachtet (in unseren Experimenten das Bild eines Objekts), wird die Kompassnadel stabiler und damit präziser. Zusammen liefern diese Ergebnisse neue Einblicke darüber, wie das Gehirn visuelle Orientierungspunkte nutzt, um die Kodierung räumlicher Informationen über die Umwelt dynamisch zu verbessern.



Weitere Informationen:

Universitätsmedizin Göttingen

Klinik für Augenheilkunde

Prof. Dr. Emilie Macé, Telefon: 0551/6117

Center for Biostructural Imaging of Neurodegeneration

Von Siebold Str. 3a, 37075 Göttingen

emilie.mace@med.uni-goettingen.de

RESEARCH ARTICLE SUMMARY

NEUROSCIENCE

Visual objects refine head direction coding

Dominique Siegenthaler, Henry Denny†, Sofía Skromne Carrasco†, Johanna Luise Mayer†, Daniel Levenstein, Adrien Peyrache*‡, Stuart Trenholm*‡, Émilie Macé*‡



Full article and list of author affiliations: <https://doi.org/10.1126/science.adu9828>

INTRODUCTION: In our day-to-day life, we use visual objects (e.g., a specific clock tower when walking around town, etc.) as spatial landmarks to help orientate ourselves as we make our way through the world. We can use visual objects as spatial landmarks because our brains dedicate considerable computational power toward parsing the world into objects. Moreover, our location in the world is processed by specialized cells such as place cells, grid cells, and head direction (HD) cells in the brain's spatial navigation system. However, much remains unknown about how visual objects modulate tuning properties of the neurons that encode spatial variables, partly because it is unclear how visual objects are processed in the rodent brain, where spatial navigation signals have been most extensively studied.

RATIONALE: To address this gap in knowledge, we reasoned that a brainwide activity screen in mice could identify visual object–preferring areas in an unbiased way. Using electrophysiology, we then characterized the spatial correlates of individual neurons in the areas responding to objects in freely moving mice.

RESULTS: Our brainwide screen based on functional ultrasound imaging revealed that spatial navigation–related areas, not visual cortical areas, tended to show a preference for visual objects. The postsubiculum, a hub of the HD system, exhibited the strongest object preference. In head-fixed conditions, we

discovered that HD cells were differentially modulated by visual stimulation based on their preferred firing direction: HD cells pointing toward the visual stimulus were excited, whereas HD cells pointing away from the visual stimulus were inhibited. The same modulation was observed in freely moving conditions, when an object was displayed in the environment.

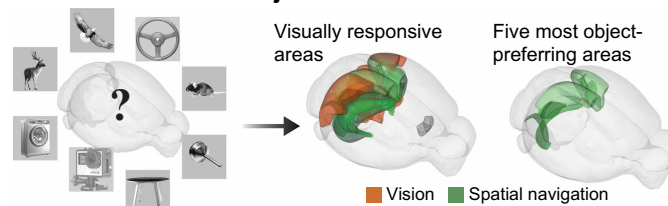
CONCLUSION: Visual objects refine the population encoding of HD in the postsubiculum by increasing the response of HD cells that code toward the object while simultaneously decreasing the firing rate of HD cells that code directions away from the object. As an analogy, imagine yourself wandering around a city with a compass (which, in our experiments, is the brain's HD system), and each time you look at a landmark (which, in our experiments, is an image of an object), the compass needle becomes more stable and thus more accurate. Together, these results provide insights into how the brain uses visual landmarks to dynamically enhance the encoding of spatial information about the world. □

*Corresponding author. Email: adrien.peyrache@mcgill.ca (A.P.); stuart.trenholm@mcgill.ca (S.T.); emilie.mace@med.uni-goettingen.de (E.M.) †These authors contributed equally to this work. ‡These authors contributed equally to this work. Cite this article as D. Siegenthaler *et al.*, *Science* **389**, eadu9828 (2025). DOI: [10.1126/science.adu9828](https://doi.org/10.1126/science.adu9828)

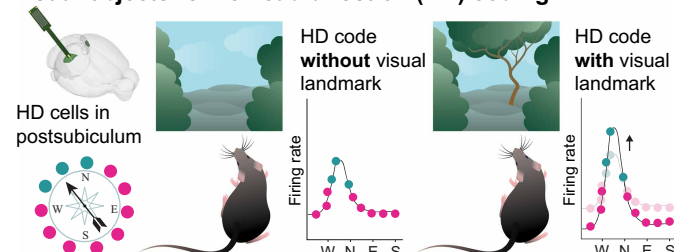
Visual objects sharpen the representation of head direction.

Of all visually responsive regions, the most object-preferring areas belonged to the spatial navigation system. Electrophysiological analysis in one of the identified regions, the postsubiculum, indicated that when an animal faces a visual landmark, HD encoding is refined. W, west; N, north; E, east; S, south. [Three-dimensional brain images prepared with cocoframer © 2018 Allen Institute for Brain Science. Allen Brain Explorer]

Brainwide screen for object areas in the mouse brain



Visual objects refine head direction (HD) coding



NEUROSCIENCE

Visual objects refine head direction coding

Dominique Siegenthaler^{1,2,3,4,†}, Henry Denny^{4,†},
Sofia Skromne Carrasco^{4,‡}, Johanna Luise Mayer^{1,2,3,‡},
Daniel Levenstein^{4,5,§}, Adrien Peyrache^{4,*¶}, Stuart Trenholm^{4,*¶},
Émilie Macé^{1,2,3,*¶}

Animals use visual objects to guide navigation-related behaviors. However, visual object–preferring areas have yet to be described in the mouse brain, limiting our understanding of how visual objects affect spatial navigation system processing. Using functional ultrasound imaging, we identified brain areas that were preferentially activated by images of objects compared with their scrambled versions. Whereas visual cortex did not show a preference, areas associated with spatial navigation were preferentially activated by visual objects. Electrophysiological recordings in postsubiculum, the cortical head direction (HD) system hub, confirmed a preference for visual objects in both HD cells and fast-spiking interneurons. In freely moving animals, visual objects increased firing rates of HD cells aligned with a visual object but decreased activity in HD cells coding for other directions.

The spatial navigation system is composed of neurons whose firing rate is modulated by variables that include the direction an animal is facing and the location it occupies in an environment (1–3). These neurons are believed to support the generation of a cognitive map (4, 5). In addition to spatial variables, spatial navigation system neurons are modulated by visual inputs (6), given that visual objects (7) can serve as environmental landmarks (8). Moving a visual landmark in an environment can result in a corresponding shift in the tuning of head direction (HD) cells (9), place cells (10, 11), and grid cells (3). Furthermore, placing an animal in the dark can lead to tuning instability (12, 13). Thus, visual landmarks can anchor the internal representation of space (14). Nonetheless, although some previous work has investigated the influence of vision on neuron firing in spatial navigation areas (15–18), much remains unknown about how visual objects modulate the way neurons in the spatial navigation system encode spatial information.

Although spatial navigation systems have been best examined in the rodent brain, studies on visual object processing have been performed primarily in primates (19). This has revealed a series of brain areas, arranged in a hierarchical manner and referred to as the “ventral visual stream,” that are tasked with encoding increasingly high-level representations of visual objects (19, 20). In rodents, lateral visual cortical areas appear to exhibit certain ventral stream–like properties (21–24), and rodents can perform behavioral tasks that rely on view-invariant visual object recognition (22, 25, 26). However, it remains unknown whether, like primates, rodents possess brain areas that

are more strongly driven by objects than other types of visual stimuli. Additionally, little is known about whether visual object processing overlaps with brain areas known to contain neurons that encode spatial variables.

Results

A brainwide screen for areas that preferentially respond to visual objects

To begin, we performed a brainwide screen in mice using functional ultrasound (fUS) imaging (27–29) to search for areas that responded preferentially to visual objects. Mice were implanted with a COMBO cranial window (30) and head-fixed under the ultrasound probe (Fig. 1A). Visual stimuli were presented while fUS signals were measured simultaneously from almost the whole mouse brain (excluding olfactory bulbs, cerebellum, and parts of the hindbrain). Images were presented 60° in height, centered along the horizontal meridian and 20° above the vertical meridian (Fig. 1A), a part of the visual field thought to be particularly behaviorally relevant for mice (31) and that has been hypothesized to be important for processing visual landmarks (32). To cover a large part of object space (33), a set of 48 different objects from different object categories were shown (fig. S1). For image scrambling, we used a texture-scrambling method (34–36) (Scrambled_T) which destroyed object identity but maintained low-level images statistics. The 48 images were split into four blocks of 12 images and four blocks of corresponding Scrambled_T images, where each block lasted for 12 s to allow reliable detection of visually evoked changes in blood volume (Fig. 1B and fig. S1).

First, we examined the visual response, in anesthetized mice, to all eight blocks (i.e., combining object and scrambled stimuli). We found visual stimulus–evoked activity in voxels throughout the mouse brain (Fig. 1C). After anatomically segmenting the brain into ~100 areas, we found visual activity in 27 brain areas (fig. S1). We computed a visual object sensitivity index (VOSI_T), to quantify preferences for object versus Scrambled_T images (see Materials and methods). VOSI_T analysis revealed a small number of brain areas with a statistically significant preference for visual objects: the postsubiculum (PoSub), parasubiculum, and area prostriata (Fig. 1, D to F). By contrast, many areas, including V1, did not exhibit a preference for objects or scrambled images (Fig. 1, D to F). One area, the superior colliculus (SC), responded significantly stronger to Scrambled_T images (Fig. 1, D to F). We found largely similar results when we repeated experiments in awake animals, with SC responding significantly more strongly to Scrambled_T images and PoSub responding significantly stronger to objects (fig. S2, A to D).

To examine whether there was a systematic bias for visual object sensitivity at the level of brain systems, we rank-ordered visually responsive brain areas according to their VOSI_T values. Based on the literature, we categorized visually responsive brain areas as belonging to either (i) the visual system, (ii) the spatial navigation system, or (iii) other (Fig. 1G and table S3). Within the top 10 areas with the highest VOSI_T values, eight were closely associated with the spatial navigation system (Fig. 1G), and the average VOSI_T value of all visually responsive spatial navigation–related areas was significantly larger than zero (Fig. 1H). We obtained a similar result from recordings in awake animals, with spatial navigation areas exhibiting higher VOSI_T values than visual areas (fig. S2, E and F). If instead we used unsupervised clustering approaches based solely on visually evoked responses to object and scrambled stimuli, brain areas and voxels of visually responsive spatial navigation areas clustered together and exhibited a preference for visual objects over Scrambled_T images (fig. S3).

Finally, because visual object processing in mouse cortex may be biased toward ventral visual cortical areas (21, 22), we subdivided the “visual system” group into ventral and dorsal visual cortical areas. We did not detect a difference in activation by object versus scrambled images for either ventral or dorsal visual cortical areas (fig. S4).

¹Brain-Wide Networks Group, Department of Ophthalmology, University Medical Center Göttingen, Else Kröner Fresenius Center for Optogenetic Therapies, Göttingen, Germany.

²Cluster of Excellence “Multiscale Bioimaging: From Molecular Machines to Networks of Excitable Cells” (MBExC), University of Göttingen, Germany. ³Brain-Wide Circuits for Behavior Research Group, Max Planck Institute for Biological Intelligence, Planegg, Germany. ⁴Montreal Neurological Institute, McGill University, Montreal, QC, Canada. ⁵Mila, Montreal, QC, Canada. *Corresponding author. Email: adrien.peyrache@mcgill.ca (A.P.); stuart.trenholm@mcgill.ca (S.T.); emilie.mace@med.uni-goettingen.de (E.M.) †Present address: Institute of Molecular and Clinical Ophthalmology Basel, Basel, Switzerland. ‡These authors contributed equally to this work. §Present address: Department of Neuroscience, Yale School of Medicine, New Haven, CT, USA. ¶These authors contributed equally to this work.

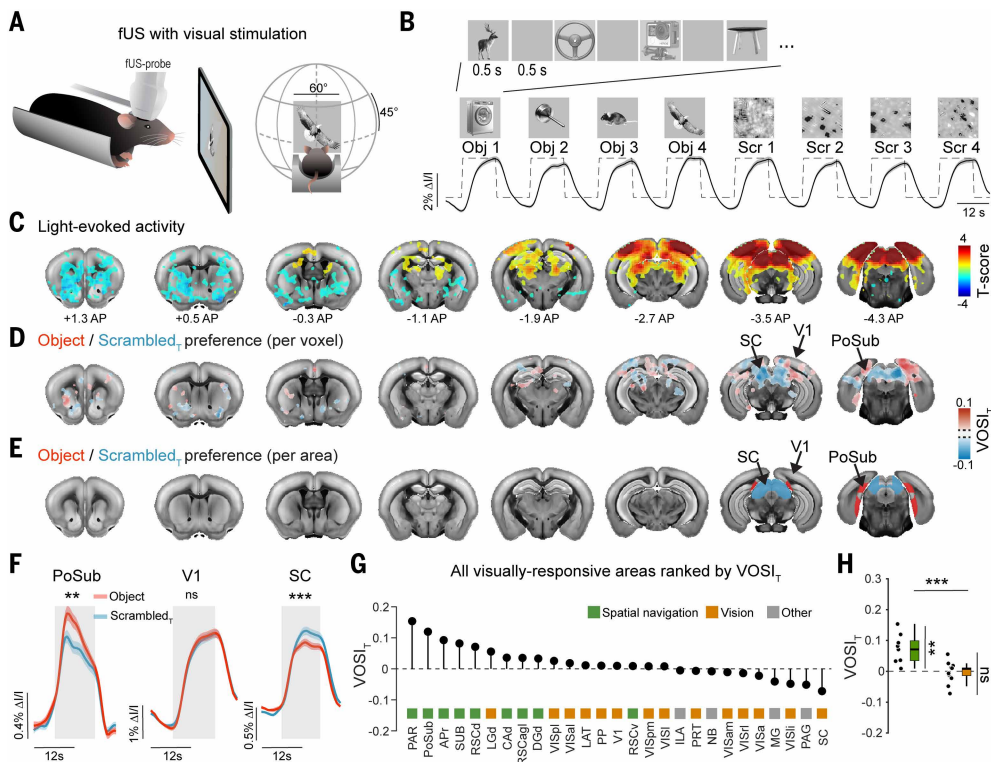


Fig. 1. Visual object-sensitive brain areas revealed with brainwide fUS imaging. (A) Schematic of fUS imaging with visual stimulation. (B) At the top is a schematic of the stimulus design, with blocks of object and scrambled images interleaved with full-field gray stimuli. At the bottom are pooled fUS responses (mean \pm SEM) from V1 for each stimulus block ($n = 56$ sessions from seven anesthetized animals; the same data were used for all analyses in this figure). (C) Visually evoked fUS responses (all image blocks as regressors) overlaid on coronal brain images at indicated positions. Only T-scores that are significantly different from zero are shown; $p < 0.05$ using false discovery rate (FDR)-corrected, mixed-effects model. (D) Visually active voxels color coded by $VOST_T$ values are displayed on coronal brain images (only absolute $VOST_T$ values greater than 0.015 are shown). (E) Brain areas with a $VOST_T$ significantly different from zero are colored by their $VOST_T$ values; $p < 0.05$ using FDR-corrected, mixed-effects model. (F) Average fUS responses to Object and Scrambled_T images, from PoSub, V1, and SC. From left to right, $p = 0.001$ (**), 0.359 (ns), and 6.3×10^{-7} (***) using Bonferroni-Holm (B-H)-corrected, mixed-effects model. (G) Rank ordering of visually responsive brain areas according to $VOST_T$ values (black dots), color-coded (squares) according to spatial navigation (green), vision (orange) or other (gray) brain networks. (H) $VOST_T$ values of all brain areas belonging to either spatial navigation (green) or vision networks (orange). For statistical comparison between the two networks, $p = 7.5 \times 10^{-4}$ (***) using Mann-Whitney U test. $VOST_T$ values for spatial navigation, but not vision, networks statistically differed from zero. p (spatial navigation, green) = 0.008 (***) and p (vision, orange) = 0.952 (ns) using B-H-corrected, one-sample Wilcoxon signed-rank test. For box-and-whisker plots, the center line represents the median, box limits are upper and lower quartiles, and whiskers are minimum and maximum values excluding outliers (below $Q1 - 1.5 \times IQR$ and above $Q3 + 1.5 \times IQR$). ns, not significant.

A preference for visual objects in postsubicular neurons

To ensure that visual object preferences identified with fUS were driven by neuronal firing (37), we performed acute electrophysiological recordings from several brain areas in head-fixed anesthetized mice (Fig. 2A and fig. S5). We recorded from areas of the spatial navigation system: PoSub (which had a positive $VOST_T$ in fUS), as well as dorsal and ventral retrosplenial cortex (RSCd and RSCv). We chose RSC because, from our fUS experiments, RSCd, but not RSCv, trended toward preferring object images. Additionally, RSC is a spatial navigation area involved with processing visual landmarks (15, 38). As controls, we recorded from two visual areas: V1 and SC. We presented animals with the same object images as in fUS experiments but now included a second form of scrambling, diffeomorphic transformation (39), which maintains overall object shape while modifying local pixel-level spatial organization (Scrambled_D; Fig. 2B and fig. S6).

We compared fUS recordings to single-unit spike recordings, first focusing on the difference between responses to objects and Scrambled_T images (Fig. 2, C to E). For single-cell responses, we tested for a

preference for visual objects by subtracting the response to Scrambled_T images from the response to objects (Object-Scrambled_T). Neurons in PoSub and RSCd exhibited a preference for visual objects. Neurons in SC, V1, and RSCv cortex did not exhibit a preference for visual objects, although, in accordance with the fUS results, there was a negative trend in the SC Object-Scrambled_T response (Fig. 2D). For all five areas, spiking recapitulated fUS preferences for object versus Scrambled_T images, with a strong correlation between the object preferences calculated with both recording modalities [Fig. 2E; Pearson's correlation coefficient ($R = 0.97$)]. Next, we examined responses to diffeomorphic transformations (Fig. 2, F to H). From this point forward, we considered brain areas to prefer visual objects only if they showed a preference for objects over both Scrambled_T and Scrambled_D. This was the case for PoSub and RSCd (Fig. 2, G and H). By contrast, V1, RSCv, and SC did not show a preference for objects (Fig. 2, G and H). General feature preferences of neurons in these five areas to other visual stimuli are shown in fig. S7.

In PoSub, HD and fast-spiking cells exhibit a preference for visual objects

How do visual objects modulate the processing of spatial information? Because PoSub was one of the most visual object-preferring areas in both our screens, and because it possesses HD cells (2, 40) and is modulated by visual landmarks (14), we focused further on this area. To obtain freely moving recordings and head-fixed visual stimulation recordings from the same neurons, we chronically implanted a silicon probe in PoSub (fig. S8). We introduced mice to an open-field arena, with a single visual landmark on the

wall (Fig. 3A). Immediately after open-field recordings, animals were kept awake, moved to a different part of the room, head-restrained in front of a computer monitor, and shown the same set of natural visual objects and control stimuli as outlined above for anesthetized animals.

First, we examined the nature of light-evoked activity in PoSub. Visual stimulation increased the firing rate of some PoSub neurons, whereas it decreased the firing rate of other neurons (Fig. 3B). Visual stimulation did not decrease the firing rate of PoSub neurons in anesthetized animals, and visually evoked responses in PoSub were more transient in awake animals and lacked an OFF response component that was present in anesthetized animals (fig. S9). From awake electrophysiological recordings, we then split PoSub neurons into positively and negatively visually modulated cells. The preference for visual objects was specific to positively visually modulated cells (Fig. 3, C and D).

Next, using the spike waveform, baseline firing rate, and HD information encoded by each cell, we classified PoSub neurons into three cell types: HD cells, fast-spiking (FS) inhibitory cells and slow non-HD cells (40) (Fig. 3E). Positively and negatively modulated cells were

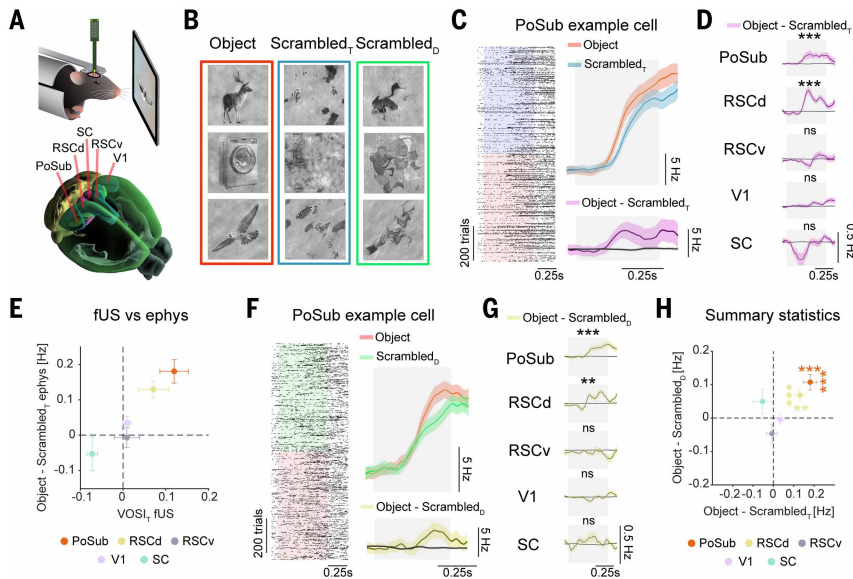


Fig. 2. A preference for visual objects in PoSub and RSCd in single-cell recordings. (A) Schematic of the experimental approach and the recording sites. [Brain schematic credit: © 2018 Allen Institute for Brain Science. Allen Brain Explorer] (B) From left to right, example Object (red box), Scrambled_T (texture; blue box), and Scrambled_D (diffeomorphic transformations; green box) images. (C) On the left is a raster plot showing spiking responses from a single neuron in PoSub to Object (red) and Scrambled_T (blue) images. At the top right are the mean (solid line) ± SEM (shaded area) responses to Object (red) and Scrambled_T (blue) images from the same cell. At the bottom right are the mean (solid line) ± SEM (shaded area) response differences of Object-Scrambled_T responses. The black solid line with shaded area shows the mean ± SEM for 100 permutations. (D) Traces of Object-Scrambled_T (purple line, mean ± SEM across cells). Shuffled response distribution is shown for visualization purposes (black line, mean ± SEM of 100 permutations of trial labels shuffling). From top to bottom, $p = 1.2 \times 10^{-8}$ (***), 1.2×10^{-5} (***), 0.205 (ns), 0.205 (ns), and 0.176 (ns) using B-H-corrected, Wilcoxon signed-rank test (from top to bottom, $n = 192, 120, 81, 145,$ and 61 cells). (E) Object preference compared with Scrambled_T stimuli for all five areas calculated using fUS data (VOSI_T, x axis, mean ± SEM, $n = 56$ sessions) and ephys data [Object-Scrambled_T, y axis, mean ± SEM, n values are the same as in (D)]. (F and G) The same as (C) and (D), except for Object versus Scrambled_D; from top to bottom, $p = 1.2 \times 10^{-6}$ (***), 0.007 (**), 0.447 (ns), 0.456 (ns), and 0.456 (ns) using B-H-corrected, Wilcoxon signed-rank test [n values are the same as in (D)]. (H) Object-Scrambled_T and Object-Scrambled_D values for neurons from the five different brain areas [mean ± SEM; n and p values are the same as in (D) and (G) for the brain areas].

present in each group. However, most negatively modulated cells were HD cells (Fig. 3F). Focusing solely on positively modulated cells, we found that a preference for visual objects (i.e., positive Object-Scrambled_T and positive Object-Scrambled_D responses) was present in HD cells and FS cells, but not in slow non-HD cells (Fig. 3, G to I).

Visual stimulation modulates firing rates of HD cells as a function of preferred firing direction

We next examined whether there was a relationship between the differential effects of visual stimulation on the firing rate of PoSub HD cells and their preferred firing directions. We focused on PoSub HD cells because FS cells possess more complex tuning curves (40). For a given animal, we calculated the preferred firing direction of all simultaneously recorded HD cells and positioned each HD cell on a ring, with the angular position of each cell corresponding to its preferred firing direction (Fig. 4A). Next, for the same HD cells, we calculated each cell's visual response from the head-fixed recordings. We observed a clustering of positive responses on the ring. Pairs of positively visually modulated HD cells had preferred firing directions that were more similar than pairs of HD cells with opposite responses to the visual stimulation (Fig. 4, A and B). However, because the HD tuning curves above were calculated in one environment and the head-fixed recordings

were performed in a different environment, it was unclear how the preferred firing directions that were calculated in the freely moving condition related to the animal's head-fixed HD. We therefore took advantage of existing knowledge about population responses in the HD system. The HD system exhibits several hallmarks of a continuous ring attractor (41). First, only HD cells with similar preferred firing directions can be active at a given time, resulting in a localized “bump of activity” in the ring (5, 42). Second, the angular offset between pairs of HD cells is maintained across different environments (43), making it possible to compare responses of similarly tuned neurons between different conditions. We tested whether the skewed distribution of positively and negatively visually responsive HD cells around 360° related to the bump of activity in the HD ring attractor calculated in head-fixed animals. Because HD cells continue to fire even when an animal is stationary (2, 44), the bump of activity in baseline firing should indicate which HD cells are encoding the animal's head-fixed HD. The bump of activity in the HD network closely aligned with the region of the ring that exhibited positive visual responses (Fig. 4, C and D), meaning that HD cells pointing toward the visual stimulus, directly in front of the mouse, were the ones positively modulated by the visual stimulus. This also means that the absence of object preference in negatively responding cells (Fig. 3D) could simply result from low firing rates, which compress the differential effect between object and scrambled images.

To further examine the link between visual response and HD tuning, we realigned the ring for each mouse so that the region enhanced with positively visually modulated cells was centered at 0° (Fig. 4E). We found a correlation between visual response and angular position on the ring across all the cells recorded in different animals compared with shuffled data (Fig. 4E and fig. S10, A to D). After realignment, the preferred firing directions for negatively responding HD cells were significantly farther away from 0° than the preferred firing directions of positively responding cells (Fig. 4F). Furthermore, HD cells whose preferred firing directions pointed toward 0° (preferred firing direction of $0^\circ \pm 40^\circ$ after realignment) exhibited stronger visual responses than the remaining HD cells (preferred firing direction of $180^\circ \pm 140^\circ$ after realignment; Fig. 4G and fig. S10E).

However, not every positively visually responding HD cell had a preferred firing direction aligned with the visual cue. We wondered whether this is related to “imperfections” in HD tuning curves, because although many HD cells are exclusively tuned to only a single HD, some exhibit a second peak, usually with a lower peak firing rate than the dominant peak. Indeed, tuning curves of positively visually responding cells with preferred directions not aligned with the visual cue possessed tuning curves that were less uniformly distributed than positively responding cells with preferred directions aligned with the visual cue (fig. S10F). Restricting the analysis described in Fig. 4D to include only HD cells with a single peak in their HD tuning curves enhanced the effect and revealed that cells with a preferred firing direction of $180^\circ \pm 140^\circ$ respond significantly negatively to the visual cue (fig. S10, G to J).

Next, we asked whether our finding of a differential effect of visual input on HD cell firing as a function of preferred firing direction could arise from an untuned input, as we hypothesized that it is unlikely that the visual input reaching PoSub would already be tuned by HD.

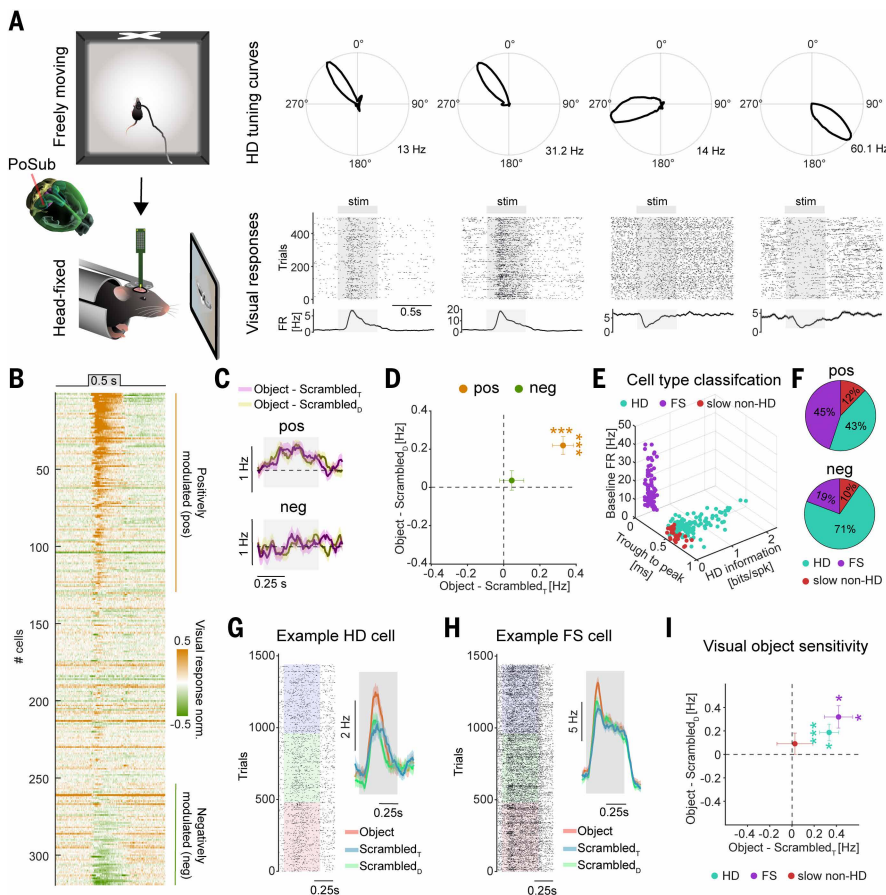


Fig. 3. A preference for visual objects is present in HD and FS neurons in PoSub. (A) On the left is a schematic of the two awake experimental paradigms. In the freely moving condition, the wall-mounted landmark was a white X. On the right are polar plots for four simultaneously recorded HD cells in the PoSub (top) and responses of the same cells to 500 randomly selected visual stimulus presentations (bottom), plotted both as raster plots and as a mean visually evoked firing rate (FR). [Brain schematic credit: © 2018 Allen Institute for Brain Science. Allen Brain Explorer] (B) The average visually evoked responses of all cells recorded in the PoSub in awake animals ($n = 319$ cells from five animals), ordered by visual response strength. Cells significantly visually modulated are highlighted on the right. (C) Mean (solid line) \pm SEM (shaded area) across positively or negatively modulated cells for Object-Scrambled_T and Object-Scrambled_D responses [$n = 129$ (pos) and 65 (neg) cells]. (D) Object-Scrambled_T and Object-Scrambled_D values for positively and negatively visually modulated PoSub neurons (mean \pm SEM); $p(\text{Object-Scrambled}_T, \text{orange}) = 4.5 \times 10^{-7}$ (***) and $p(\text{Object-Scrambled}_T, \text{green}) = 0.978$ (ns), and $p(\text{Object-Scrambled}_D, \text{orange}) = 1 \times 10^{-4}$ (***) and $p(\text{Object-Scrambled}_D, \text{green}) = 0.947$ (ns) using B-H-corrected, Wilcoxon signed-rank test [$n = 129$ (orange) and 65 (green) cells]. (E) PoSub neurons from freely moving recordings grouped into three categories (FS, HD, and slow non-HD), based on baseline firing rate, spike waveform (trough to peak), and HD information (bits per spike). (F) Cell-type distributions for negatively and positively modulated cells. (G) Example raster plots (left) and mean \pm SEM firing rate (right) of an example PoSub HD cell in awake conditions in response to Object, Scrambled_D, and Scrambled_T stimuli. (H) Same as (G), but for an example FS neuron. (I) Object-Scrambled_T and Object-Scrambled_D values for different types of positively modulated PoSub neurons (mean \pm SEM); $p(\text{Object-Scrambled}_D, \text{cyan}) = 0.049$ (*), $p(\text{Object-Scrambled}_D, \text{violet}) = 0.014$ (*), and $p(\text{Object-Scrambled}_D, \text{red}) = 0.566$ (ns), and $p(\text{Object-Scrambled}_T, \text{cyan}) = 8.1 \times 10^{-4}$ (***) , $p(\text{Object-Scrambled}_T, \text{violet}) = 0.014$ (*), and $p(\text{Object-Scrambled}_D, \text{red}) = 0.938$ (ns) using B-H-corrected, Wilcoxon signed-rank test [$n = 42$ (cyan), 44 (violet) and 12 (red) cells].

We reasoned that a supralinear stabilized network (SSN) might recapitulate our observation, as SSNs have previously accounted for tuning-specific experimental results when model units were organized in a ring architecture (45, 46) and the SSN activity properties differ depending on the strength of the input (45). Here, the units of the SSN were provided with a spatially localized bump of activity, modeling activity within the HD ring attractor representing the current HD (Fig. 4, H to J). We examined the effect of the visual input to PoSub, modeled as an untuned input to the ring SSN network (Fig. 4K). Despite

the visual input to all units being the same, it evoked differential effects depending on each model unit's angular distance from the current HD (Fig. 4L). The model recapitulated the experimental data, with visual input producing an increase in firing of model units coding for the animal's current HD and a decrease in firing of model units coding HDs away from the current HD. These results were robust to parameter variations (fig. S11). This effect arose only when visual stimulation corresponded to a decrease in global input to the SSN.

Visual objects dynamically refine population-level encoding of HD in freely moving mice

The visual stimulation experiments described in the previous sections were performed in head-fixed conditions. Do visual objects similarly modulate HD cell firing in freely moving conditions? To test this—in the open-field arena with a single, wall-mounted visual landmark—we restricted our analysis to time points when the mouse was either directly facing the landmark (On landmark; Fig. 5A) while making sure to match the distributions of HDs included in the two conditions (fig. S12). Because in freely moving conditions eye movements are strongly linked to head movements and mostly serve to stabilize the visual field (47–51), our analysis used the animal's HD as a proxy for its direction of gaze. We then subtracted the average Off landmark firing rate from the average On landmark firing rate and normalized to the Off landmark firing rate to obtain a “visual response” value in freely moving conditions. The visual response of HD cells with preferred firing directions that were aligned with the direction of the landmark ($0^\circ \pm 40^\circ$) was significantly larger than the visual response of HD cells that coded for directions not aligned with the landmark ($180^\circ \pm 140^\circ$; Fig. 5B). This arose because the firing rate of HD cells aligned with the landmark ($0^\circ \pm 40^\circ$) was boosted when the mouse faced the landmark (Fig. 5C), whereas the firing rate of HD cells not aligned with the landmark ($180^\circ \pm 140^\circ$) was decreased when the mouse faced the landmark (Fig. 5D).

Because in head-fixed conditions PoSub HD cells responded more strongly to objects than scrambled images, we examined whether this preference for objects was maintained during freely moving conditions. We recorded from HD cells in an arena containing two wall-mounted visual landmarks, 180° offset from each other, with one landmark being a randomly selected object from the set that we used in our head-fixed experiments and the other landmark being the diffeomorphic scramble of that object (Fig. 5E). We measured the visual response, as described in the previous paragraph, for the object landmark and for the scrambled landmark. We found a significant modulation by the object landmark (Fig. 5F) but not the scrambled landmark (Fig. 5G).

Discussion

Combining brainwide fUS imaging and both head-fixed and freely moving electrophysiological recordings in mice, we made two central

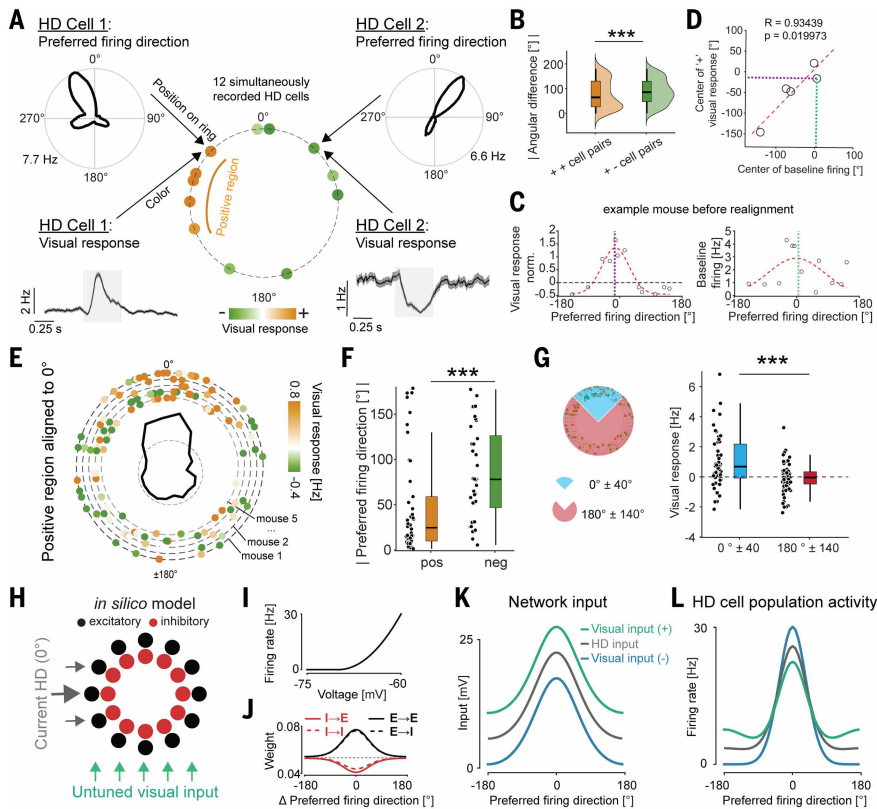


Fig. 4. Visual stimulation differentially modulates HD cells as a function of preferred firing direction. (A) Schematic outlining how, for each mouse, we compared the visual response and preferred firing direction for all simultaneously recorded HD cells. The preferred firing direction is indicated by the angular position of each cell (dot) on the ring, and the visual response is indicated by the dot color (orange, positive; green, negative). Data for this panel were shifted by 60° for visualization purposes [unshifted data from the same mouse are shown on the left side of (C)]. (B) The angular difference in preferred firing directions for pairs of HD cells that were statistically positively modulated by visual stimulation (orange) and for pairs of HD cells where one cell was positively visually modulated and the other cell negatively visually modulated (green); $p = 4.1 \times 10^{-5}$ (***) using Mann-Whitney U test [$n = 508$ (orange) and 876 (green) pairs of cells]. (C) For an example mouse, the visual response (normalized to baseline firing rate) as a function of HD preferred firing direction (left) and baseline firing rate (in head-fixed) as a function of HD preferred firing direction (right). Violet and green dotted lines represent the circular mean for the example mouse. (D) For each mouse, the circular mean of positive visual responses is plotted against the circular mean of baseline firing ($n = 5$ mice). (E) Rings (dashed circles with colored dots) are shown for five mice, with the center of the positive visual response regions aligned to 0°. In the center, the dashed ring represents the mean visual response across all bins and the bold line the deviations from it (20 angular bins). (F) Absolute preferred firing direction for positively and negatively modulated cells; $p = 5 \times 10^{-4}$ (***) using Mann-Whitney U test [$n = 42$ (orange) and 37 (green) cells]. (G) Comparison between the visual responses of HD cells with preferred firing directions $0^\circ \pm 40^\circ$ (blue) or $180^\circ \pm 140^\circ$ (red); $p = 1.3 \times 10^{-4}$ (***) using Mann-Whitney U test [$n = 50$ (blue) and 77 (red) cells]. (H) Excitatory and inhibitory neurons are assigned a preferred HD at which they receive the strongest tuned input (current HD input). In addition, all neurons receive an untuned input (visual input). (I and J) Neurons in the network have a supralinear activation function (I), and their local weights are determined by the difference in their preferred firing direction (J). Weight and activation function parameters were set following Hennequin *et al.* (46) and were varied to verify model robustness (see fig. S11). (K and L) Increasing or decreasing the level of untuned input (K) has a differential effect on model HD cell firing rates (L), depending on whether the preferred HD is in-field (current HD: 0°), or out-field (180°). For box-and-whisker plots, the center line represents the median, box limits are upper and lower quartiles, and whiskers are minimum and maximum values excluding outliers (below $Q1 - 1.5 * IQR$ and above $Q3 + 1.5 * IQR$).

findings related to visual objects and the brain's spatial navigation system. First, at the level of mean activity in brain areas, visually responsive spatial navigation areas exhibit a preference for visual objects over scrambled versions of the same images. Second, visual inputs directly modulate HD coding in PoSub: Visual objects boost the firing rate of HD cells with preferred firing directions pointing toward the

object and decrease the firing rate of HD cells that encode other HDs.

Unlike in humans and nonhuman primates (52, 53), our brainwide screen did not reveal that ventral visual cortical areas were more strongly activated by objects than by scrambled images. Although it is possible that spatial resolution limitations imposed by volumetric fUS (~250 μm) and image registration constraints could impede our ability to detect visual object preferences in particularly small brain areas, our findings are consistent with single-cell calcium imaging experiments from mouse ventral stream areas that have failed to reveal individual neurons with preferred stimuli that resemble objects (24). However, the lack of a clear preference for visual objects in the rodent ventral pathway does not mean that neurons in these areas are not involved in encoding visual objects. Studies in rodents found that the amount of view-invariant object information increased along the ventral stream hierarchy (21, 22). Furthermore, in mouse V1, although phase scrambling natural images does not affect mean population activity or response variance, it does affect higher-order correlations between neurons (42). Thus, although mouse visual cortex appears capable of encoding information about visual objects and passing this information onto the spatial navigation system, unlike primates, there may not be specific visual cortical areas dedicated to encoding visual objects. Interestingly, beyond a potential role in visual object processing, it has been hypothesized that the rodent ventral visual stream may be important for visually guided spatial navigation, as ventral visual cortical areas mostly encode regions of the visual field directly in front of the mouse, which could help them process visual landmarks (32).

Owing to the hemodynamic readout of fUS (which is relatively slow and likely requires that many neurons in a given brain area show light-evoked activity in order to be detected with fUS) and how we pooled together different objects in stimulus blocks, it is possible that our screen might have missed other brain areas with highly selective responses to only a fraction of the objects or missed areas possessing a low percentage of visual object-preferring cells. For example, the medial entorhinal cortex contains object-vector cells driven by vision (17, 54), as well as visual cue selective cells (16), but it did not appear visually responsive in our fUS screen [or in previous brainwide visual screens performed with fUS (28, 30, 55) or functional magnetic resonance imaging (fMRI) (56)], indicating limitations that should be taken into consideration when using such hemodynamic-based approaches to perform screens for visually responsive brain areas.

Our experiments demonstrate that several areas within the spatial navigation system, notably RSCd and PoSub, are visually responsive [which builds on other work showing auditory and whisker responses in the HD system (57)] and preferentially respond to visual objects. Both of these areas are known to receive substantial input from the visual system and to be involved with the processing of landmarks (14, 58, 59). RSC is critical for aligning reference frames, translating egocentric signals into allocentric information, including the HD signal (59, 60). RSC

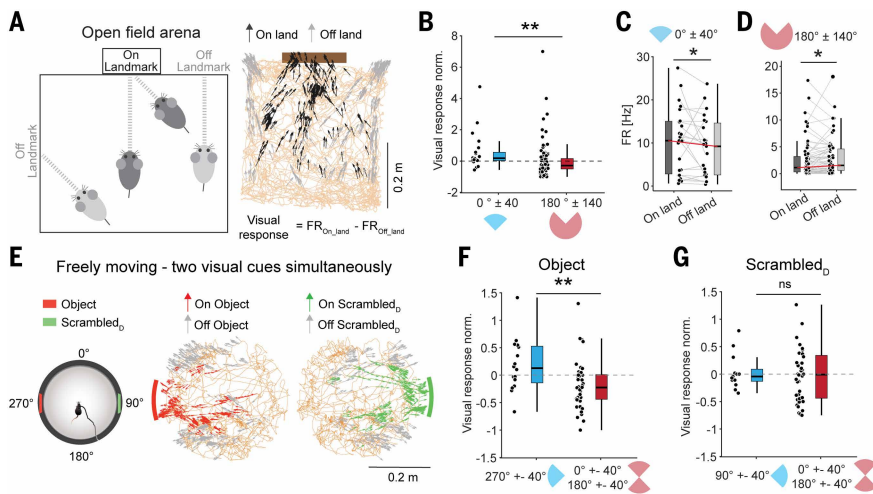


Fig. 5. Visual objects dynamically refine population-level HD encoding. (A) On the left is a schematic illustrating how for HDs toward the wall containing the visual landmark, from some positions, the mice look directly at the landmark (On landmark), whereas from other positions, the mice do not directly look at the landmark (Off landmark). On the right, the location over time is shown (orange) for one mouse, with HDs colored by whether the mouse's view is On landmark (black arrows) or Off landmark (gray arrows). The visual cue is represented by the thick brown line. (B) Normalized visual responses in freely moving conditions for HD cells with preferred firing directions within the range of $0^\circ \pm 40^\circ$ and $180^\circ \pm 140^\circ$; $p = 0.003$ (**) using Mann-Whitney *U* test [$n = 22$ (blue) and 105 (red) cells]. (C) For HD cells with preferred firing directions within the range of $0^\circ \pm 40^\circ$, the average firing rate (FR) for both On and Off landmark (land) positions is shown; $p = 0.0495$ (*) using Wilcoxon signed-rank test ($n = 22$ cells). (D) Same as (C) for cells with preferred firing directions within the range $180^\circ \pm 140^\circ$; $p = 0.029$ (*) using Wilcoxon signed-rank test ($n = 105$ cells). (E) In a subset of mice, recordings were performed in an open-field arena containing two visual landmarks: one object and one diffeomorphic scrambled version of the same object. As in (A), time points when the mice were facing the landmarks (On object and On Scrambled₀) and a matched distribution of HDs where the mice were not looking at the landmark (Off object and Off Scrambled₀) were extracted. (F) The normalized visual responses elicited by the object were significantly higher for cells with preferred firing direction in the direction of the object; $p = 0.008$ (***) using Mann-Whitney *U* test [$n = 16$ (blue) and 41 (red) cells]. (G) The refinement effect in (F) was not observed for visual responses elicited by the diffeomorphic scrambled version of the object; $p = 0.733$ (ns) using Mann-Whitney *U* test [$n = 13$ (blue) and 41 (red) cells].

detects visual landmarks in the environment and integrates them with subcortical HD inputs, which are primarily driven by vestibular and proprioceptive signals, anchoring the HD signal to the external world (38, 61–65). PoSub is the cortical hub of the HD system (66) and updates the HD signal with visual orientation cues (9, 67). It broadcasts the HD signal to downstream navigation structures such as the medial entorhinal cortex and hippocampus (68). Although the HD signal is ubiquitous in the medial entorhinal cortex (69, 70), hippocampal neurons also show tuning to HD in the presence of salient visual cues (71). We found other areas of the spatial navigation system that were modulated by visual objects, and it is possible that visual objects affect HD coding in those other areas as well. For example, our fUS screen identified the parasubiculum as preferring visual objects, and this area plays a role in conveying a directional signal to spatially tuned cells of the entorhinal cortex (72). We also found a preference for visual objects in area prostriata, which is located between V1 and the hippocampal formation and is involved in processing fast, moving stimuli in the peripheral visual field (73, 74), which could provide fast access to spatial information (73, 75).

The preference for visual objects in the spatial navigation system that we describe does not appear to result from highly specific responses to individual objects by individual neurons. Instead, it appears to reflect a general preference for objects over scrambled images, which could arise from a preference for natural spatial image statistics present in objects. This object preference could be useful for isolating

objects from a noisy, visually cluttered environment and facilitate the use of visual objects as spatial landmarks. This preference for visual objects was present in both awake and anesthetized conditions, similar to what has been found in the inferior temporal cortex of primates (76). Future work will be required to investigate how optic flow, which can also affect coding of HD (77), relates to object modulation of HD cells. Furthermore, because the preference for visual objects was maintained in anesthetized conditions, it indicates that the response preference in spatial navigation areas represents a sensory driven phenomenon. Similarly, in awake conditions, we did not find a significant difference in pupil diameter for object versus scrambled images (fig. S13), consistent with the interpretation that the preference for visual objects is not simply an attentional signal. Lastly, whereas the anatomical connectivity between primary visual cortex, higher visual areas, and RSC and PoSub is well mapped out (58, 59, 78–80), the specific pathways and computations that enable visual objects to get encoded and modulate the spatial navigation system remain to be elucidated.

Materials and methods

Animals

Experiments performed in Germany complied with the institutional guidelines of the Max Planck Society and were approved by the local government (Regierung von Oberbayern). Experiments performed in Canada were done in accordance with the Canadian Council on Animal Care and approved by the Montreal Neurological Institute's Animal Care Committee. Male and female C57BL/6 mice aged 4–12 weeks were used in all experiments. They were housed in groups under a 12-hour light-dark cycle with unrestricted access to standard diet and water.

Cranial window surgery

Surgeries were performed as described previously (30). Briefly, mice were anesthetized with a subcutaneous injection of fentanyl (0.05 mg/kg), midazolam (5 mg/kg), and medetomidine (0.5 mg/kg) (FMM cocktail). They were secured using a bite bar and kept at 37°C with a temperature controller (Supertech). To prevent their eyes from drying, a hydration gel (Bayer, Bepanthen) was applied. A large cranial window was created in the skull using a dental drill, extending from bregma +2.25 mm AP to bregma -4.00 mm AP, while ensuring the dura remained intact. A pre-prepared COMBO window (30) was adhered to the exposed bone using cyanoacrylate glue (Pattex) and the contact was reinforced with dental cement (Super-Bond). Anesthesia was reversed after surgery by administering subcutaneous flumazenil (0.5 mg/kg) and atipamezole (2.5 mg/kg). Postoperative analgesia was managed with subcutaneous injections of buprenorphine (0.1 mg/kg). After a 7-day recovery period, the FMM cocktail was administered again, a head plate was attached to the COMBO window, and the anesthesia was reversed by a cocktail of flumazenil (0.5 mg/kg), atipamezole (2.5 mg/kg), and naloxone (1.2 mg/kg). Mice were allowed at least 3 days of additional recovery before being gradually acclimated to the experimenter, the behavioral setups, and tasks.

Habituation to head fixation

For awake fUS recording sessions, all animals underwent gradual habituation to a head-fixed context. For the first 1 to 2 days, they were

allowed to explore the behavior rig. Over the next 5+ days, the duration of head fixation increased daily from 10 min to 60 min.

fUS acquisition

fUS-imaging data was collected using a 32×32 channel matrix probe (15 MHz, 1024 total elements, spatial resolution: $220 \times 280 \times 175 \mu\text{m}^3$, Vermon) connected to a Vantage 256 system (Verasonics, Inc.) and controlled by a custom volumetric fUS acquisition module (AUTC). A 4x multiplexer linked the 1024 channel probe to the 256-channel system, with the beamforming and sequences adjusted accordingly. For fUS recordings under anesthesia, mice were injected with the FMM cocktail and kept at 37°C with a temperature controller. Next, the mouse was head-fixed in a holding tube and the matrix probe was positioned to cover the entire cranial window using a three-way translation stage. A compound ultrasound image was created from the summation of plane wave emissions at -4.5° , -3° , -1.5° , 0° , 1.5° , 3° , and 4.5° . A power Doppler image was generated from the incoherent average of 160 compound ultrasound images acquired at 400 Hz. Clutter filtering was performed in real time by decomposing the ultrasound stack using singular value decomposition, removing the first 20% of singular vectors. This resulted in a power Doppler image approximately every 500 ms.

Electrophysiology recordings under anesthesia

Data was recorded at 20 kHz using RHX software from 32-channel silicon probes (Cambridge NeuroTech, type HI0b) connected via a SPI interface cable (Intan technologies, C3216) to a USB interface board (Intan technologies, C3100). Mice were anesthetized with the FMM cocktail and head-fixed in a holding tube, aligned to the probe manipulator's coordinate system. Small perforations (0.5 mm diameter) were made above the region of interest, and the probe was lowered into the brain at 2 $\mu\text{m/s}$. Recordings began 10 min after reaching the target depth. For separate recordings on different days, perforations were sealed with Kwik-Cast silicone sealant. CM-Dii (Thermo Fisher, CellTracker) was applied to the probe before brain insertion to identify recording sites post hoc.

Silicon probe implantation for chronic (awake) electrophysiology

Animals were anesthetized with 5% isoflurane and positioned in a stereotaxic apparatus. Anesthesia during the surgery was maintained with 1.5-2% isoflurane. Animals were given a subcutaneous saline injection (~0.8 ml) and carprofen (20 mg/kg), as well as a subcutaneous 1:1 lidocaine-bupivacaine mixture underneath the incision site as soon as they were placed in the stereotaxic apparatus.

A thin layer of light-cured adhesive (Kerr OptiBond) was applied to the skull to help implants better adhere to the skull. A head-fixation bar was cemented to the skull using a dental acrylic cement (Unifast Trad). A silver wire was then implanted into the cerebellum to serve as a reference electrode. Two types of silicon probes were utilized for the experiments: a single-shank probe (Cambridge NeuroTech H5) or a single shank probe with a Molex connector (Cambridge NeuroTech H5). Both probes were mounted on a moveable microdrive.

A craniotomy was performed above the target area, creating a hole slightly larger than the probe itself, approximately 0.1 mm wider on each side. The silicon probes were implanted to the following coordinates: AP (from Lambda) +0.30, ML -2.35 , DV -1.10 . The probe was carefully lowered into position and affixed to the skull using dental acrylic cement (Unifast Trad). To minimize electrical interference during recordings, a copper mesh was attached to the skull surrounding the implant using a light-cured flowable composite (Fusion Flo).

After surgery, animals were given a second subcutaneous saline injection (~0.8 ml) and placed on a heated pad until fully recovered. Post-surgery, animals were housed individually and received daily carprofen injections for at least three days. Animals were allowed to recover for 7 days post-surgery before further experimentation.

Electrophysiological recordings in awake animals

The probe was lowered slowly into the postsubiculum using the microdrive over the course of 2-3 hours. Brain tissue was allowed to recover for 2 hours before the start of the recording. Neurophysiological signals were recorded continuously at 20 kHz using a 256-channel RHD USB Interface board (Intan Technologies) and captured with Intan RHX software.

Behavior of the mouse during freely moving open field arena sessions was tracked using reflective markers that were mounted on the copper mesh or pre-amplifier. These were tracked in 3D with infrared cameras and Motive 2.0 motion capture system (Optitrack). Video was captured by an additional camera mounted overhead. Behavioral tracking was acquired at a rate of 120 Hz and synchronized with the electrophysiological signal using voltage pulses registered by the RHD USB Interface Board. The mice were allowed to roam freely in a circular or square environment for 15-20 min. Following the freely moving session, animals were immediately head-fixed and presented with the visual stimulation task.

Visual stimulation

Images were presented at a size of 60° with the center of the image at 0° azimuth and $+20^\circ$ elevation on a 61 cm computer monitor (Dell, U2415b) using the PsychoPy toolbox. The monitor was placed 18 cm in front of the mouse. For fUS experiments, we employed a block design consisting of 12 s of gray followed by 12 s of images (12 images, each presented for 0.5 s interleaved with 0.5 s gray, with images presented in random order across trials). Each recording run consisted of eight repetitions of eight blocks (four object blocks and four texture scrambling blocks) in pseudorandom order. For object presentation in electrophysiological experiments, images (48 objects, 48 textures, 48 diffeomorphic transformations) were presented in pseudorandom order for 10 times for 0.5 s and interleaved with at least 0.5 s of gray.

Image preparation

Original images were resized to 1024×1024 pixels and put on a medium gray background. For each of these images we created a control image with matching statistics using the described texture synthesis algorithm (36) with 25 iterations. Briefly, this algorithm generates a scrambled image by matching a multitude of parameters (variance, kurtosis, oriented linear filter responses and many more) of local features in the starting image without taking into account the spatial position of these local features [see also <https://www.cns.nyu.edu/~lcv/texture/> and (34) for a detailed description of the algorithm]. Subsequently, all images were gamma corrected and the SHINE toolbox (81) was used to luminance match all images. Finally, to avoid edge effects a small border (7 pixels around the image) was blurred using a Gaussian filter. For stimuli used in electrophysiological experiments we additionally created a second set of control images (diffeomorphic transformations) using a previously published algorithm (39). Briefly, diffeomorphic transformations are constructed by iteratively applying a flow field derived from a set of two-dimensional cosine components, each with random phase and amplitude. As in this algorithm, each pixel is expanded or contracted with the same probability, the scrambled image contains similar number of foreground (object) pixels at comparable spatial locations. Additionally, to avoid potential changes in spatial frequency or luminance content introduced by this procedure, for electrophysiology experiments with two scrambling methods, the whole amplitude spectra (specMatch.m) as well as the luminance histogram (histMatch.m) of all images and their respective controls were equated in ten iterations using the SHINE toolbox.

Pupil size

During functional ultrasound recordings in awake, head-fixed animals the pupil of one eye was video recorded. For this an IR light was placed near the mouse and a monochrome camera (Blackfly S) with an IR filter

was pointed at the eye of the mouse. Videos were triggered using PsychoPy at the beginning of the visual stimulation and frames were collected at 10 Hz. For analysis, FaceMap (82) was used to extract the pupil size. For each session the extracted pupil size was z-scored and at the individual trial level the pupil size before image onset was subtracted. Next, the average fluctuation of pupil size during all trials of object image presentation or all Scrambled_T images was determined. Then, the mean pupil size before stimulus onset was subtracted from the mean pupil size during stimulus presentation to get an average pupil response of the whole session for either Object or Scrambled_T images.

Data analysis

All analysis was performed using MATLAB (Mathworks) or Python.

fUS preprocessing

The fUS time series was first registered to the Allen Brain Institute's mouse brain atlas. For this, first all sessions of a mouse were aligned using an automated approach based on the MATLAB `imregtform.m` function. Then, a high-resolution power Doppler image was created by averaging 100 fUS frames from a single session, which was manually registered to the atlas using anatomical landmarks to create a transformation matrix using a previously published toolbox (29). This matrix was applied to data from other sessions of the same mouse. The fUS time series was preprocessed using custom MATLAB scripts on a voxel-by-voxel basis. Temporal interpolation was performed to achieve a constant frame rate of 2 Hz. The relative change in power Doppler signal was calculated by subtracting the baseline signal from each time point and dividing by the baseline signal. Slow drifts were removed using a fifth-order high-pass Butterworth filter with a cutoff frequency of 0.056 Hz. To eliminate movement artifacts during awake experiments, the top 10% of temporal principal components extracted from non-brain voxels was regressed out from all voxels.

fUS activation

To assess brain activation at the voxel-wise level, the preprocessed fUS data was temporally smoothed (four frames) and fitted using a General Linear Model (GLM) using the MATLAB function `glmfit.m`. Model regressors included the visual stimulation block stimuli, convolved with a single-gamma hemodynamic response function. The resulting T-scores were averaged across animals/sessions and plotted on top of the Allen Brain Atlas (thresholded by *p* values, see below).

To assess activation at the brain area level, first the preprocessed and trial-averaged (only trials of the same type of stimulus; objects or texture) whole-brain data was segmented into individual brain areas. For this, anatomical areas from the Allen reference brain atlas were consolidated into 100 brain areas and the data from all voxels within each area was averaged. Next, the correlation coefficient between the stimulus timing and the fUS signal of each brain area was calculated. To not remove areas that only respond to object or texture blocks respectively, the correlation was performed three times (objects only, scrambled only and both combined). Areas with significant *p* values (see below) for one or more of the three correlations were defined as active.

Similarly, to find brain areas with differences between object and scrambled stimuli, a preference index for each area (or voxel) was calculated on the preprocessed and trial-averaged fUS data. For this, the area under the curve during the response window for texture stimuli was subtracted from the response to object stimuli and normalized by the sum of the two responses (VOSI_T). To unbiasedly define a response window for each area/voxel, we averaged all data of a given experiment (sessions, animals, stimuli, all trials) to end up with a single response kernel. The start of the response window was defined as the point with maximum rate of change. The end of the response was defined as the point where the response dropped below 70% of the peak response (30% for awake fUS data due to different temporal dynamics). In case this method did not result in a meaningful response window

(window very short or start/stop point before/after stimulus onset/offset), a generic stimulus window (from stimulus onset to stimulus offset) was used.

To determine significance, a mixed effects model was fitted on T-scores, correlation scores or preference indices for each area/voxel using the MATLAB `fitlme.m` function. Resulting *p* values were corrected for multiple comparisons using false discovery rate (FDR) correction.

Area and voxel clustering

Preprocessed, segmented, and trial-averaged (trials of the same stimulus type) fUS data of visually active areas were clustered using a MATLAB UMAP (83) implementation (Meehan, Version 4.4; with correlation as distance metric and the following parameters: `n_neighbors=5`, `cluster_detail='very low'`). Similarly, for hierarchical clustering, the segmented and trial-averaged fUS data of visually active areas was clustered using the MATLAB function `dendrogram.m` (distance metric = correlation, linkage method = weighted). For clustering at the level of voxels, preprocessed and trial-averaged fUS data of visually active voxels (defined by the above described GLM approach) were clustered using k-means with correlation as distance metric and number of clusters defined by the silhouette method.

Preprocessing electrophysiology

Electrophysiological recordings were processed with Kilosort3, and the spike sorting results were manually refined using the Phy software (<https://github.com/cortex-lab/phy>). Only units that exhibited stable responses throughout the session and achieved high Kilosort quality scores were included in the analysis. To estimate continuous firing rates, single-unit responses were binned with a 10 ms bin size and in for some analysis smoothed using a Gaussian kernel with 10 ms SD. Except for raster plots, the ten trials of the same image were averaged. Raster plots were plotted using the Gramm toolbox (84).

Visual object and scrambled stimuli

To select only visually responsive units, we averaged all trials and stimuli of a cell, temporally smoothed the response (10 ms window) and determined the response amplitude as the difference of the peak of this overall averaged response minus the baseline firing rate. Cells with an amplitude below 1 Hz were excluded from the analysis (in awake electrophysiology all cells were included). To determine the difference between object and control stimulus presentation, the average firing rate during the response window (stimulus onset to stimulus offset) was calculated and the median response to control stimuli (Scrambled_T or Scrambled_D) was subtracted from the median response to object.

Receptive field mapping

White squares (30° × 30° visual angle) were flashed at 15 different positions (three elevation positions × five azimuth positions) of the screen at random order. Each position was repeated 20 times. The stimulus was presented for 0.5 s followed by at least 0.5 s of gray. Only units that had a response amplitude larger than 1 Hz for at least one of the screen positions were included in the analysis. To determine how many positions of the screen resulted in a significant activation, we tested at each position whether the firing rates during the response (40 ms around peak response) was significantly different from the firing rates before and after stimulus presentation across the 20 repetitions of the stimulus (Wilcoxon signed rank test, B-H corrected).

Spatial frequency tuning

Black and white striped stimuli of different spatial frequencies and two orientations (horizontal and vertical) were presented at random order. Like object stimuli, the area of these stimuli spanned 60° visual angle and were centered at 0° azimuth and +20° elevation, and were displayed for 0.5 s, interleaved with 0.5 s full-field gray. Each stimulus was shown 20 times. Only units with a significant response to at least

one stimulus (Wilcoxon signed rank test, FDR corrected) were included in the analysis. For each cell and spatial frequency, the maximum firing rate during the response window in response to the more preferred orientation was calculated. This resulted in a per cell spatial frequency tuning curve (the maximum represents the preferred spatial frequency) that, for visualization of units with different firing rates, was rescaled between 0 and 1.

Chirp stimulus

A full-field temporal chirp stimulus was presented 20 times, interleaved with 10 s of full-field gray. The stimulus intensity smoothly transitioned from black to white with increasing frequency from around 0.3 Hz up to 4 Hz. Only units with a response amplitude larger than 3 Hz were included for analysis. To determine when a cell stopped responding to the chirp stimulus, first, the normalized firing rates of each cell were decomposed in time-frequency using 1-D wavelet transformation (MATLAB `cwt.m` function). Then, the power across all frequencies was summed and the point in time during the stimulus where the power dropped below 1.5 times of the pre-stimulus power was calculated. The last chirp frequency presented before this time point represents the maximal frequency the cell responded to.

HD tuning metrics

HD tuning curves were calculated as previously described (40). Briefly, markers on the animal's headcap were tracked and connected to a three-dimensional polygon allowing calculation of head direction as the horizontal orientation (yaw) of the polygon. The yaw was measured in global coordinates (i.e., aligned with the environment's axes, which remained consistent throughout the study). HD tuning curves were generated by taking the ratio of histograms of spike counts to the total time spent in each direction, using 1° bins and smoothing with a Gaussian kernel (3° standard deviation). The preferred firing direction of a cell is defined as the mean direction of the tuning curve.

To determine how strongly a cell is tuned to head direction, for each cell we determined the head direction information as previously described (40) with this formula:

$$I = \sum_{i=1}^n \lambda(\Theta_i) \log_2 \left[\frac{\lambda(\Theta_i)}{\lambda} \right] p(\Theta_i)$$

Here, n represents the total number of angular bins and $\lambda(\Theta_i)$ represents the firing rate of the cell in the i th angular bin, λ denotes the neuron's overall average firing rate during exploration, and $p(\Theta_i)$ indicates the occupancy (normalized time spent) in direction Θ_i . The information rate (I , expressed in bits per second) was then adjusted by the neuron's average firing rate to yield an information content metric (head direction information, measured in bits per spike).

Cell-type classification

PoSub cells were classified as previously described (40). Briefly, cells with a baseline firing rate larger than 10 Hz (during freely moving condition) and a trough to peak duration shorter than 0.4 ms were classified as fast-spiking neurons. In contrast, cells with baseline firing rates below 10 Hz and trough to peak duration above 0.4 ms were considered slow-spiking neurons. This group was further subdivided into HD cells (head direction information above 0.1 bit/spk) or slow non-HD cells (head direction information below 0.1 bit/spk). All other cells were not classified.

Visual responses in head-fixed conditions and realigning HD based on visual responses

To determine whether a cell was positively or negatively modulated by visual stimulation, the mean firing rate during the stimulus presentation was compared to the firing rate during stimulus OFF period across all trials of a cell using a Wilcoxon signed rank test. Cells with corrected p values (B-H correction) smaller than 0.05 and a mean

positive response were assigned to the positively modulated group (and accordingly for negatively modulated cells). To visualize the visual responses with respect to the cell's HD direction tuning (activity bump, center ring in Fig. 4E), the realigned cells of all mice were binned into 20 angular bins based on their preferred head direction. Then the smoothed and binned visual responses were plotted as scaled deviation (0.1 scaling factor) from the average response (dashed line circle).

In each mouse we observed an accumulation of cells with similar head direction tuning and increased visual activity (and baseline activity), however the center of this activity was differently oriented for each mouse likely because there was no systematic remapping when moving the mice from the freely moving condition to the head-fixation setup. As such, we realigned the HD cells' preferred directions such that the cluster of positively visually modulated HD cells was centered around 0°. For this, in each mouse the circular mean of the preferred directions of the cells that positively responded to the visual stimulus was determined, and this mean direction was subtracted from the preferred directions of all cells, concurrently shifting the whole ring. For shuffled distributions, the realignment process per mouse was repeated 100,000 times, with the visual responses of all cells of a mouse randomly shuffled and the preferred directions kept constant. To calculate the center of baseline firing in head-fixed condition, the circular mean of the cells with high baseline firing rate (> median of all cells of a mouse) was determined.

Visual responses in freely moving mice with one landmark

Positional and head direction data was resampled to match 25 ms binning of the spiking data (MATLAB `resample.m`). Then, to identify time points when the mouse was looking directly at the visual landmark (On landmark) or looking away from the landmark (Off landmark), at each spatial location we checked if and where the extension of the head direction immediately in front of the animal intersected with the landmark (the landmark consisted of white "X" with width 16.5 cm). In one of the five mice used for the single landmark experiment (Fig. 5, A to C) the experiment was performed in a circular arena and the landmark consisted of a white square with the width of 21.5 cm. Spatial locations and head directions with intersections on the landmark (but not on the edges: 1 cm buffer zone) were considered "On landmark." Similarly, spatial locations and head directions with intersections beside the landmark were considered "Off landmark." To ensure the intersections were "Off landmark," intersections closer than 10 cm from a landmark edge were excluded. To exclude positions and head directions with extreme cue viewing angles, which would result in a strong distortion of visual cue, in both cases, only time points, where the absolute head direction was $0^\circ \pm 45^\circ$ were included. Moreover, to ensure that the selection of the time points did not result in a bias in selection of head directions (which could result in differences between "Off landmark" and "On landmark" due to HD tuning of the cells), we subsampled the larger of the two indices and matched the histogram of head directions for each session. Finally, we averaged the firing rates during "On landmark" (FR_{ON}) and "Off landmark" (FR_{OFF}) time points and calculated the normalized visual response for each cell as $(FR_{ON} - FR_{OFF})/FR_{OFF}$.

Visual responses in freely moving mice and two landmarks

The same steps were used as above, except that the visual cues were affixed on two wall locations 180° offset from each other. Moreover, the visual cues were images of an object and diffeomorphic scrambled image of the same object exactly as used in the visual stimulation experiment (objects were placed on a gray background). The width of the printout was 21.5 cm and the object or scrambled object were 13 cm wide. Due to this, only time points that intersected with the actual object on the printout were considered "On landmark," while only time points beside the printout were considered "Off landmark." For both landmark locations (in our relative framework), these were centered at 270° (object) and 90° (Scrambled) as above to ensure only reasonable

viewing angles, only time points where the head direction pointed more or less straight at the cue ($\pm 45^\circ$) were included. Also as described above, head directions for On and Off landmark were matched and the average firing rates during On or Off landmark were determined and the normalized visual response was calculated. Due to the setup of this experiment with two visual cues present at the same time, cells with preferred firing direction aligned with the object (270° -pointing cells) were different cells compared to cells with preferred firing direction aligned with the diffeomorphic scrambled image (90° -pointing cells). However, cells with preferred firing directions non-aligned with the visual cues were the same in both cases (0° - and 180° -pointing cells).

Response delay

For each HD cell, all trials and stimuli presentations were averaged to get an overall response of the cell. The response delay was defined as the point when the firing rate of the cell rose above two times the standard deviation of the pre-stimulus period.

Perfusion and histology

Following the termination of the electrophysiological experiments, animals were deeply anesthetized using sodium pentobarbital or ketamine (120 mg/kg) and xylazine (16 mg/kg) cocktail and perfused transcardially first with 0.9% phosphate-buffered saline solution followed by 4% paraformaldehyde solution.

In case of chronic recordings, the microdrive was retracted to remove the probe from the brain. Then brains were isolated and kept in a 4% paraformaldehyde solution for 24 hours, after which the solution was changed to 30% sucrose in phosphate-buffered saline until sinking. After freezing in a -80°C freezer, brains were sectioned with a freezing microtome coronally in $40\ \mu\text{m}$ slices. Sections were washed, counterstained with DAPI and mounted on glass slides with ProlongGold fluorescence antifade medium. Sections containing probe tracts were additionally incubated with a Cy3 anti-mouse secondary antibody (1:200 dilution; Cedarlane, 715-165-150) to help visualize the electrode tract. Widefield fluorescence microscope (Leica) was used to obtain images of sections and verify the tracks of silicon probe shanks.

In case of acute recordings, after perfusion, brains were collected and incubated in 4% PFA at 4°C overnight. Then brains were washed and embedded in 4% agarose. Coronal slices were cut using a vibratome (Leica microsystems, VT1000S) with a thickness of $100\ \mu\text{m}$ and stained with DAPI (Thermo Fisher Scientific, D1306 or R37606). Brain slices were washed and mounted on microscope slides in Vectashield (Vector Laboratories, H-1200). Images were captured using a Leica TCS SP8 laser scanning confocal microscope with a $20\times$ air objectives (Leica Microsystems). Images were processed using LAS X (Leica Microsystems) and Adobe Photoshop software.

SSN model

The supralinear stabilized ring network model followed (46). Specifically, the network contained $N_E = 50$ excitatory and $N_I = 50$ inhibitory neurons evenly spaced around a ring with angle $\theta \in [-\pi, \pi]$. The circuit dynamics followed

$$\tau_\theta \frac{dV_\theta}{dt} = -V_\theta + V_{rest} + h_\theta + \sum_{\theta' \in \text{Ecells}} W_{\theta\theta'} r(V_{\theta'}) - \sum_{\theta' \in \text{Icells}} W_{\theta\theta'} r(V_{\theta'})$$

where V_θ and τ_θ correspond to the membrane potential and time constant of a model unit at angle θ , V_{rest} is the neuronal resting potential, h_θ is the external input, and $W_{\theta\theta'} \propto \exp\left[\frac{\cos(\theta-\theta')-1}{\ell_{syn}^2}\right]$ is the strength of synaptic connection from neuron θ' to neuron θ , which is further scaled such that the sum of incoming weights corresponds to W_{EE} , W_{IE} , $-W_{EI}$ and $-W_{II}$. The input was taken to be

$$h_\theta(\theta_{stim}) = I + A_{max} \exp\left[\frac{\cos(\theta-\theta_{stim})-1}{\ell_{stim}^2}\right]$$

which consists of a tuned component at $\theta_{stim} = 0$ with half width ℓ_{stim} and magnitude A_{max} , and an untuned component of magnitude I . We assumed that E and I model units at a given HD are driven equally strongly by the stimulus.

Finally, the firing rate of each cell is a threshold-power law function of its membrane potential:

$$r(V_\theta) = k[V_\theta - V_0]_+^n$$

Parameters were taken as the default in (46) (see table S7). To test the parameter robustness of our results, a population of 1250 networks with different weight hyperparameters was sampled from a uniform distribution (see table S7 for bounds). For each of these networks, the change in rate of neurons aligned with the input HD (0° , corresponding to the current HD; “in-field”) and opposite to that HD (180° ; “out-field”) was calculated for a small change in input ($dI = 0.1$).

REFERENCES AND NOTES

1. J. O'Keefe, J. Dostrovsky, The hippocampus as a spatial map. Preliminary evidence from unit activity in the freely-moving rat. *Brain Res.* **34**, 171–175 (1971). doi: [10.1016/0006-8993\(71\)90358-1](https://doi.org/10.1016/0006-8993(71)90358-1); pmid: [5124915](https://pubmed.ncbi.nlm.nih.gov/5124915/)
2. J. S. Taube, R. U. Muller, J. B. Ranck Jr., Head-direction cells recorded from the postsubiculum in freely moving rats. I. Description and quantitative analysis. *J. Neurosci.* **10**, 420–435 (1990). doi: [10.1523/JNEUROSCI.10-02-00420.1990](https://doi.org/10.1523/JNEUROSCI.10-02-00420.1990); pmid: [2303851](https://pubmed.ncbi.nlm.nih.gov/2303851/)
3. T. Hafting, M. Fyhn, S. Molden, M.-B. Moser, E. I. Moser, Microstructure of a spatial map in the entorhinal cortex. *Nature* **436**, 801–806 (2005). doi: [10.1038/nature03721](https://doi.org/10.1038/nature03721); pmid: [15965463](https://pubmed.ncbi.nlm.nih.gov/15965463/)
4. E. C. Tolman, Cognitive maps in rats and men. *Psychol. Rev.* **55**, 189–208 (1948). doi: [10.1037/h00061626](https://doi.org/10.1037/h00061626); pmid: [18870876](https://pubmed.ncbi.nlm.nih.gov/18870876/)
5. B. L. McNaughton, F. P. Battaglia, O. Jensen, E. I. Moser, M.-B. Moser, Path integration and the neural basis of the ‘cognitive map’. *Nat. Rev. Neurosci.* **7**, 663–678 (2006). doi: [10.1038/nrn1932](https://doi.org/10.1038/nrn1932); pmid: [16858394](https://pubmed.ncbi.nlm.nih.gov/16858394/)
6. A. B. Saleem, L. Busse, Interactions between rodent visual and spatial systems during navigation. *Nat. Rev. Neurosci.* **24**, 487–501 (2023). doi: [10.1038/s41583-023-00716-7](https://doi.org/10.1038/s41583-023-00716-7); pmid: [37380885](https://pubmed.ncbi.nlm.nih.gov/37380885/)
7. J. Feldman, What is a visual object? *Trends Cogn. Sci.* **7**, 252–256 (2003). doi: [10.1016/S1364-6613\(03\)00111-6](https://doi.org/10.1016/S1364-6613(03)00111-6); pmid: [12804691](https://pubmed.ncbi.nlm.nih.gov/12804691/)
8. E. Chan, O. Baumann, M. A. Bellgrove, J. B. Mattingley, From objects to landmarks: the function of visual location information in spatial navigation. *Front. Psychol.* **3**, 304 (2012). doi: [10.3389/fpsyg.2012.00304](https://doi.org/10.3389/fpsyg.2012.00304); pmid: [22969737](https://pubmed.ncbi.nlm.nih.gov/22969737/)
9. J. S. Taube, R. U. Muller, J. B. Ranck Jr., Head-direction cells recorded from the postsubiculum in freely moving rats. II. Effects of environmental manipulations. *J. Neurosci.* **10**, 436–447 (1990). doi: [10.1523/JNEUROSCI.10-02-00436.1990](https://doi.org/10.1523/JNEUROSCI.10-02-00436.1990); pmid: [2303852](https://pubmed.ncbi.nlm.nih.gov/2303852/)
10. R. U. Muller, J. L. Kubie, The effects of changes in the environment on the spatial firing of hippocampal complex-spike cells. *J. Neurosci.* **7**, 1951–1968 (1987). doi: [10.1523/JNEUROSCI.07-07-01951.1987](https://doi.org/10.1523/JNEUROSCI.07-07-01951.1987); pmid: [3612226](https://pubmed.ncbi.nlm.nih.gov/3612226/)
11. K. J. Jeffery, Learning of landmark stability and instability by hippocampal place cells. *Neuropharmacology* **37**, 677–687 (1998). doi: [10.1016/S0028-3908\(98\)00053-7](https://doi.org/10.1016/S0028-3908(98)00053-7); pmid: [9705005](https://pubmed.ncbi.nlm.nih.gov/9705005/)
12. K. Asumbala, A. Peyrache, S. Trenholm, Flexible cue anchoring strategies enable stable head direction coding in both sighted and blind animals. *Nat. Commun.* **13**, 5483 (2022). doi: [10.1038/s41467-022-33204-0](https://doi.org/10.1038/s41467-022-33204-0); pmid: [36123333](https://pubmed.ncbi.nlm.nih.gov/36123333/)
13. T. Waaga et al., Grid-cell modules remain coordinated when neural activity is dissociated from external sensory cues. *Neuron* **110**, 1843–1856.e6 (2022). doi: [10.1016/j.neuron.2022.03.011](https://doi.org/10.1016/j.neuron.2022.03.011); pmid: [35385698](https://pubmed.ncbi.nlm.nih.gov/35385698/)
14. R. M. Yoder, B. J. Clark, J. S. Taube, Origins of landmark encoding in the brain. *Trends Neurosci.* **34**, 561–571 (2011). doi: [10.1016/j.tins.2011.08.004](https://doi.org/10.1016/j.tins.2011.08.004); pmid: [21982585](https://pubmed.ncbi.nlm.nih.gov/21982585/)
15. L. F. Fischer, R. Mojica Soto-Albors, F. Buck, M. T. Harnett, Representation of visual landmarks in retrosplenial cortex. *eLife* **9**, e51458 (2020). doi: [10.7554/eLife.51458](https://doi.org/10.7554/eLife.51458); pmid: [32154781](https://pubmed.ncbi.nlm.nih.gov/32154781/)
16. A. A. Kinkhabwala, Y. Gu, D. Aronov, D. W. Tank, Visual cue-related activity of cells in the medial entorhinal cortex during navigation in virtual reality. *eLife* **9**, e43140 (2020). doi: [10.7554/eLife.43140](https://doi.org/10.7554/eLife.43140); pmid: [32149601](https://pubmed.ncbi.nlm.nih.gov/32149601/)
17. S. O. Andersson, E. I. Moser, M.-B. Moser, Visual stimulus features that elicit activity in object-vector cells. *Commun. Biol.* **4**, 1219 (2021). doi: [10.1038/s42003-020-01566-0](https://doi.org/10.1038/s42003-020-01566-0); pmid: [33398033](https://pubmed.ncbi.nlm.nih.gov/33398033/)
18. D. Nguyen, G. Wang, T. Wafa, T. Fitzgerald, Y. Gu, The medial entorhinal cortex encodes multisensory spatial information. *Cell Rep.* **43**, 114813 (2024). doi: [10.1016/j.celrep.2024.114813](https://doi.org/10.1016/j.celrep.2024.114813); pmid: [39395171](https://pubmed.ncbi.nlm.nih.gov/39395171/)
19. J. J. DiCarlo, D. Zoccolan, N. C. Rust, How does the brain solve visual object recognition? *Neuron* **73**, 415–434 (2012). doi: [10.1016/j.neuron.2012.01.010](https://doi.org/10.1016/j.neuron.2012.01.010); pmid: [22325196](https://pubmed.ncbi.nlm.nih.gov/22325196/)
20. L. G. Ungerleider, M. Mishkin, in *Analysis of Visual Behavior*, D. J. Ingle, M. A. Goodale, R. J. W. Mansfield, Eds. (MIT Press, 1982), pp. 549–586.

21. S. Tafazoli *et al.*, Emergence of transformation-tolerant representations of visual objects in rat lateral extrastriate cortex. *eLife* **6**, e22794 (2017). doi: [10.7554/eLife.22794](https://doi.org/10.7554/eLife.22794); pmid: [28395730](https://pubmed.ncbi.nlm.nih.gov/28395730/)
22. E. Froudarakis *et al.*, bioRxiv 2020.08.20.258798 [Preprint] (2021); <https://doi.org/10.1101/2020.08.20.258798>.
23. Y. Yu, J. N. Stirman, C. R. Dorsett, S. L. Smith, Selective representations of texture and motion in mouse higher visual areas. *Curr. Biol.* **32**, 2810–2820.e5 (2022). doi: [10.1016/j.cub.2022.04.091](https://doi.org/10.1016/j.cub.2022.04.091); pmid: [35609609](https://pubmed.ncbi.nlm.nih.gov/35609609/)
24. R. Tong *et al.*, bioRxiv 2023.11.03.565500 [Preprint] (2023); <https://doi.org/10.1101/2023.11.03.565500>.
25. D. Zoccolan, N. Oertelt, J. J. DiCarlo, D. D. Cox, A rodent model for the study of invariant visual object recognition. *Proc. Natl. Acad. Sci. U.S.A.* **106**, 8748–8753 (2009). doi: [10.1073/pnas.0811583106](https://doi.org/10.1073/pnas.0811583106); pmid: [19429704](https://pubmed.ncbi.nlm.nih.gov/19429704/)
26. J. L. Hoy, I. Yavorska, M. Wehr, C. M. Niell, Vision drives accurate approach behavior during prey capture in laboratory mice. *Curr. Biol.* **26**, 3046–3052 (2016). doi: [10.1016/j.cub.2016.09.009](https://doi.org/10.1016/j.cub.2016.09.009); pmid: [27773567](https://pubmed.ncbi.nlm.nih.gov/27773567/)
27. E. Macé *et al.*, Functional ultrasound imaging of the brain. *Nat. Methods* **8**, 662–664 (2011). doi: [10.1038/nmeth.1641](https://doi.org/10.1038/nmeth.1641); pmid: [21725300](https://pubmed.ncbi.nlm.nih.gov/21725300/)
28. É. Macé *et al.*, Whole-brain functional ultrasound imaging reveals brain modules for visuomotor integration. *Neuron* **100**, 1241–1251.e7 (2018). doi: [10.1016/j.neuron.2018.11.031](https://doi.org/10.1016/j.neuron.2018.11.031); pmid: [30521779](https://pubmed.ncbi.nlm.nih.gov/30521779/)
29. C. Brunner *et al.*, Whole-brain functional ultrasound imaging in awake head-fixed mice. *Nat. Protoc.* **16**, 3547–3571 (2021). doi: [10.1038/s41596-021-00548-8](https://doi.org/10.1038/s41596-021-00548-8); pmid: [34089019](https://pubmed.ncbi.nlm.nih.gov/34089019/)
30. B. J. Edelman *et al.*, The COMBO window: A chronic cranial implant for multiscale circuit interrogation in mice. *PLoS Biol.* **22**, e3002664 (2024). doi: [10.1371/journal.pbio.3002664](https://doi.org/10.1371/journal.pbio.3002664); pmid: [38829885](https://pubmed.ncbi.nlm.nih.gov/38829885/)
31. E. H. van Beest *et al.*, Mouse visual cortex contains a region of enhanced spatial resolution. *Nat. Commun.* **12**, 4029 (2021). doi: [10.1038/s41467-021-24311-5](https://doi.org/10.1038/s41467-021-24311-5); pmid: [34188047](https://pubmed.ncbi.nlm.nih.gov/34188047/)
32. A. B. Saleem, Two stream hypothesis of visual processing for navigation in mouse. *Curr. Opin. Neurobiol.* **64**, 70–78 (2020). doi: [10.1016/j.conb.2020.03.009](https://doi.org/10.1016/j.conb.2020.03.009); pmid: [32294570](https://pubmed.ncbi.nlm.nih.gov/32294570/)
33. P. Bao, L. She, M. McGill, D. Y. Tsao, A map of object space in primate inferotemporal cortex. *Nature* **583**, 103–108 (2020). doi: [10.1038/s41586-020-2350-5](https://doi.org/10.1038/s41586-020-2350-5); pmid: [32494012](https://pubmed.ncbi.nlm.nih.gov/32494012/)
34. N. C. Rust, J. J. Dicarlo, Selectivity and tolerance (“invariance”) both increase as visual information propagates from cortical area V4 to IT. *J. Neurosci.* **30**, 12978–12995 (2010). doi: [10.1523/JNEUROSCI.0179-10.2010](https://doi.org/10.1523/JNEUROSCI.0179-10.2010); pmid: [20881116](https://pubmed.ncbi.nlm.nih.gov/20881116/)
35. N. C. Rust, J. J. DiCarlo, Balanced increases in selectivity and tolerance produce constant sparseness along the ventral visual stream. *J. Neurosci.* **32**, 10170–10182 (2012). doi: [10.1523/JNEUROSCI.6125-11.2012](https://doi.org/10.1523/JNEUROSCI.6125-11.2012); pmid: [22836252](https://pubmed.ncbi.nlm.nih.gov/22836252/)
36. J. Portilla, E. P. Simoncelli, A parametric texture model based on joint statistics of complex wavelet coefficients. *Int. J. Comput. Vis.* **40**, 49–70 (2000). doi: [10.1023/A:1026553619983](https://doi.org/10.1023/A:1026553619983)
37. A. O. Nunez-Elizalde *et al.*, Neural correlates of blood flow measured by ultrasound. *Neuron* **110**, 1631–1640.e4 (2022). doi: [10.1016/j.neuron.2022.02.012](https://doi.org/10.1016/j.neuron.2022.02.012); pmid: [35278361](https://pubmed.ncbi.nlm.nih.gov/35278361/)
38. K. K. Sit, M. J. Goard, Coregistration of heading to visual cues in retrosplenial cortex. *Nat. Commun.* **14**, 1992 (2023). doi: [10.1038/s41467-023-37704-5](https://doi.org/10.1038/s41467-023-37704-5); pmid: [37031198](https://pubmed.ncbi.nlm.nih.gov/37031198/)
39. B. Stojanowski, R. Cusack, Time to wave good-bye to phase scrambling: Creating controlled scrambled images using diffeomorphic transformations. *J. Vis.* **14**, 6 (2014). doi: [10.1167/14.12.6](https://doi.org/10.1167/14.12.6); pmid: [25301014](https://pubmed.ncbi.nlm.nih.gov/25301014/)
40. A. J. Duszkievicz *et al.*, Local origin of excitatory-inhibitory tuning equivalence in a cortical network. *Nat. Neurosci.* **27**, 782–792 (2024). doi: [10.1038/s41593-024-01588-5](https://doi.org/10.1038/s41593-024-01588-5); pmid: [38491324](https://pubmed.ncbi.nlm.nih.gov/38491324/)
41. R. Chaudhuri, B. Gerçek, B. Pandey, A. Peyrache, I. Fiete, The intrinsic attractor manifold and population dynamics of a canonical cognitive circuit across waking and sleep. *Nat. Neurosci.* **22**, 1512–1520 (2019). doi: [10.1038/s41593-019-0460-x](https://doi.org/10.1038/s41593-019-0460-x); pmid: [31406365](https://pubmed.ncbi.nlm.nih.gov/31406365/)
42. J. J. Knierim, K. Zhang, Attractor dynamics of spatially correlated neural activity in the limbic system. *Annu. Rev. Neurosci.* **35**, 267–285 (2012). doi: [10.1146/annurev-neuro-062111-150351](https://doi.org/10.1146/annurev-neuro-062111-150351); pmid: [22462545](https://pubmed.ncbi.nlm.nih.gov/22462545/)
43. S. S. Carrasco, G. Viejo, A. Peyrache, bioRxiv 2024.06.13.598909 [Preprint] (2024); <https://doi.org/10.1101/2024.06.13.598909>.
44. J. S. Taube, R. U. Muller, Comparisons of head direction cell activity in the postsubiculum and anterior thalamus of freely moving rats. *Hippocampus* **8**, 87–108 (1998). [https://doi.org/10.1002/\(SICI\)1098-1063\(1998\)8:2<87::AID-HIP01>3.0.CO;2-4](https://doi.org/10.1002/(SICI)1098-1063(1998)8:2<87::AID-HIP01>3.0.CO;2-4); pmid: [9572715](https://pubmed.ncbi.nlm.nih.gov/9572715/)
45. D. B. Rubin, S. D. Van Hooser, K. D. Miller, The stabilized supralinear network: A unifying circuit motif underlying multi-input integration in sensory cortex. *Neuron* **85**, 402–417 (2015). doi: [10.1016/j.neuron.2014.12.026](https://doi.org/10.1016/j.neuron.2014.12.026); pmid: [25611511](https://pubmed.ncbi.nlm.nih.gov/25611511/)
46. G. Hennequin, Y. Ahmadian, D. B. Rubin, M. Lengyel, K. D. Miller, The dynamical regime of sensory cortex: Stable dynamics around a single stimulus-tuned attractor account for patterns of noise variability. *Neuron* **98**, 846–860.e5 (2018). doi: [10.1016/j.neuron.2018.04.017](https://doi.org/10.1016/j.neuron.2018.04.017); pmid: [29772203](https://pubmed.ncbi.nlm.nih.gov/29772203/)
47. N. M. Proccacci *et al.*, Context-dependent modulation of natural approach behaviour in mice. *Proc. Biol. Sci.* **287**, 20201189 (2020). doi: [10.1098/rspb.2020.1189](https://doi.org/10.1098/rspb.2020.1189); pmid: [32873203](https://pubmed.ncbi.nlm.nih.gov/32873203/)
48. D. Greer, T. Lei, A. Krysztal, Z. F. Jessen, G. W. Schwartz, Visual identification of conspecific shapes social behavior in mice. *Curr. Biol.* **35**, 287–299.e4 (2025). doi: [10.1016/j.cub.2024.11.041](https://doi.org/10.1016/j.cub.2024.11.041); pmid: [39706174](https://pubmed.ncbi.nlm.nih.gov/39706174/)
49. A. F. Meyer, J. O’Keefe, J. Poort, Two distinct types of eye-head coupling in freely moving mice. *Curr. Biol.* **30**, 2116–2130.e6 (2020). doi: [10.1016/j.cub.2020.04.042](https://doi.org/10.1016/j.cub.2020.04.042); pmid: [32413309](https://pubmed.ncbi.nlm.nih.gov/32413309/)
50. A. M. Michalek, E. T. Abe, C. M. Niell, Dynamics of gaze control during prey capture in freely moving mice. *eLife* **9**, e57458 (2020). doi: [10.7554/eLife.57458](https://doi.org/10.7554/eLife.57458); pmid: [32706335](https://pubmed.ncbi.nlm.nih.gov/32706335/)
51. C. D. Holmgren *et al.*, Visual pursuit behavior in mice maintains the pursued prey on the retinal region with least optic flow. *eLife* **10**, e70838 (2021). doi: [10.7554/eLife.70838](https://doi.org/10.7554/eLife.70838); pmid: [34698633](https://pubmed.ncbi.nlm.nih.gov/34698633/)
52. R. Malach *et al.*, Object-related activity revealed by functional magnetic resonance imaging in human occipital cortex. *Proc. Natl. Acad. Sci. U.S.A.* **92**, 8135–8139 (1995). doi: [10.1073/pnas.92.18.8135](https://doi.org/10.1073/pnas.92.18.8135); pmid: [7667258](https://pubmed.ncbi.nlm.nih.gov/7667258/)
53. N. Kanwisher, J. McDermott, M. M. Chun, The fusiform face area: A module in human extrastriate cortex specialized for face perception. *J. Neurosci.* **17**, 4302–4311 (1997). doi: [10.1523/JNEUROSCI.17-11-04302.1997](https://doi.org/10.1523/JNEUROSCI.17-11-04302.1997); pmid: [9151747](https://pubmed.ncbi.nlm.nih.gov/9151747/)
54. Ø. A. Høydal, E. R. Skytøen, S. O. Andersson, M.-B. Moser, E. I. Moser, Object-vector coding in the medial entorhinal cortex. *Nature* **568**, 400–404 (2019). doi: [10.1038/s41586-019-1077-7](https://doi.org/10.1038/s41586-019-1077-7); pmid: [30944479](https://pubmed.ncbi.nlm.nih.gov/30944479/)
55. C. Brunner *et al.*, A platform for brain-wide volumetric functional ultrasound imaging and analysis of circuit dynamics in awake mice. *Neuron* **108**, 861–875.e7 (2020). doi: [10.1016/j.neuron.2020.09.020](https://doi.org/10.1016/j.neuron.2020.09.020); pmid: [33080230](https://pubmed.ncbi.nlm.nih.gov/33080230/)
56. T. N. A. Dinh, W. B. Jung, H.-J. Shim, S.-G. Kim, Characteristics of fMRI responses to visual stimulation in anesthetized vs. awake mice. *Neuroimage* **226**, 117542 (2021). doi: [10.1016/j.neuroimage.2020.117542](https://doi.org/10.1016/j.neuroimage.2020.117542); pmid: [33186719](https://pubmed.ncbi.nlm.nih.gov/33186719/)
57. E. Blanco-Hernández, G. Balsamo, P. Preston-Ferrer, A. Burgalossi, Sensory and behavioral modulation of thalamic head-direction cells. *Nat. Neurosci.* **27**, 28–33 (2024). doi: [10.1038/s41593-023-01506-1](https://doi.org/10.1038/s41593-023-01506-1); pmid: [38177338](https://pubmed.ncbi.nlm.nih.gov/38177338/)
58. S.-L. Ding, Comparative anatomy of the prosubiculum, subiculum, presubiculum, postsubiculum, and parasubiculum in human, monkey, and rodent. *J. Comp. Neurol.* **521**, 4145–4162 (2013). doi: [10.1002/cne.23416](https://doi.org/10.1002/cne.23416); pmid: [23839777](https://pubmed.ncbi.nlm.nih.gov/23839777/)
59. A. S. Alexander, R. Place, M. J. Starrett, E. R. Chrastil, D. A. Nitz, Rethinking retrosplenial cortex: Perspectives and predictions. *Neuron* **111**, 150–175 (2023). doi: [10.1016/j.neuron.2022.11.006](https://doi.org/10.1016/j.neuron.2022.11.006); pmid: [36460006](https://pubmed.ncbi.nlm.nih.gov/36460006/)
60. S. D. Vann, J. P. Aggleton, E. A. Maguire, What does the retrosplenial cortex do? *Nat. Rev. Neurosci.* **10**, 792–802 (2009). doi: [10.1038/nrn2733](https://doi.org/10.1038/nrn2733); pmid: [19812579](https://pubmed.ncbi.nlm.nih.gov/19812579/)
61. B. J. Clark, J. P. Bassett, S. S. Wang, J. S. Taube, Impaired head direction cell representation in the anterodorsal thalamus after lesions of the retrosplenial cortex. *J. Neurosci.* **30**, 5289–5302 (2010). doi: [10.1523/JNEUROSCI.3380-09.2010](https://doi.org/10.1523/JNEUROSCI.3380-09.2010); pmid: [20392951](https://pubmed.ncbi.nlm.nih.gov/20392951/)
62. A. Bicanski, N. Burgess, Environmental anchoring of head direction in a computational model of retrosplenial cortex. *J. Neurosci.* **36**, 11601–11618 (2016). doi: [10.1523/JNEUROSCI.0516-16.2016](https://doi.org/10.1523/JNEUROSCI.0516-16.2016); pmid: [27852770](https://pubmed.ncbi.nlm.nih.gov/27852770/)
63. P.-Y. Jacob *et al.*, An independent, landmark-dominated head-direction signal in dysgranular retrosplenial cortex. *Nat. Neurosci.* **20**, 173–175 (2017). doi: [10.1038/nn.4465](https://doi.org/10.1038/nn.4465); pmid: [27991898](https://pubmed.ncbi.nlm.nih.gov/27991898/)
64. H. J. I. Page, K. J. Jeffery, Landmark-based updating of the head direction system by retrosplenial cortex: A computational model. *Front. Cell. Neurosci.* **12**, 191 (2018). doi: [10.3389/fncel.2018.00191](https://doi.org/10.3389/fncel.2018.00191); pmid: [30061814](https://pubmed.ncbi.nlm.nih.gov/30061814/)
65. S. D. Auger, S. L. Mullally, E. A. Maguire, Retrosplenial cortex codes for permanent landmarks. *PLOS ONE* **7**, e43620 (2012). doi: [10.1371/journal.pone.0043620](https://doi.org/10.1371/journal.pone.0043620); pmid: [22912894](https://pubmed.ncbi.nlm.nih.gov/22912894/)
66. J. S. Taube, The head direction signal: Origins and sensory-motor integration. *Annu. Rev. Neurosci.* **30**, 181–207 (2007). doi: [10.1146/annurev.neuro.29.051605.112854](https://doi.org/10.1146/annurev.neuro.29.051605.112854); pmid: [17341158](https://pubmed.ncbi.nlm.nih.gov/17341158/)
67. J. P. Goodridge, J. S. Taube, Interaction between the postsubiculum and anterior thalamus in the generation of head direction cell activity. *J. Neurosci.* **17**, 9315–9330 (1997). doi: [10.1523/JNEUROSCI.17-23-09315.1997](https://doi.org/10.1523/JNEUROSCI.17-23-09315.1997); pmid: [9364077](https://pubmed.ncbi.nlm.nih.gov/9364077/)
68. P. Preston-Ferrer, S. Coletta, M. Frey, A. Burgalossi, Anatomical organization of presubicular head-direction circuits. *eLife* **5**, e14592 (2016). doi: [10.7554/eLife.14592](https://doi.org/10.7554/eLife.14592); pmid: [27282390](https://pubmed.ncbi.nlm.nih.gov/27282390/)
69. F. Sargolini *et al.*, Conjunctive representation of position, direction, and velocity in entorhinal cortex. *Science* **312**, 758–762 (2006). doi: [10.1126/science.1125572](https://doi.org/10.1126/science.1125572); pmid: [16675704](https://pubmed.ncbi.nlm.nih.gov/16675704/)
70. L. M. Giocomo *et al.*, Topography of head direction cells in medial entorhinal cortex. *Curr. Biol.* **24**, 252–262 (2014). doi: [10.1016/j.cub.2013.12.002](https://doi.org/10.1016/j.cub.2013.12.002); pmid: [24440398](https://pubmed.ncbi.nlm.nih.gov/24440398/)
71. L. Acharya, Z. M. Aghajani, C. Vuong, J. J. Moore, M. R. Mehta, Causal influence of visual cues on hippocampal directional selectivity. *Cell* **164**, 197–207 (2016). doi: [10.1016/j.cell.2015.12.015](https://doi.org/10.1016/j.cell.2015.12.015); pmid: [26709045](https://pubmed.ncbi.nlm.nih.gov/26709045/)
72. A. Z. Vollan, R. J. Gardner, M.-B. Moser, E. I. Moser, bioRxiv 2024.05.16.594473 [Preprint] (2024); <https://doi.org/10.1101/2024.05.16.594473>.

73. H.-H. Yu, T. A. Chaplin, A. J. Davies, R. Verma, M. G. P. Rosa, A specialized area in limbic cortex for fast analysis of peripheral vision. *Curr. Biol.* **22**, 1351–1357 (2012). doi: [10.1016/j.cub.2012.05.029](https://doi.org/10.1016/j.cub.2012.05.029); pmid: [22704993](https://pubmed.ncbi.nlm.nih.gov/22704993/)
74. M. Tamietto, D. A. Leopold, Visual cortex: The eccentric area prostriata in the human brain. *Curr. Biol.* **28**, R17–R19 (2018). doi: [10.1016/j.cub.2017.11.006](https://doi.org/10.1016/j.cub.2017.11.006); pmid: [29316413](https://pubmed.ncbi.nlm.nih.gov/29316413/)
75. K. S. Rockland, Visual system: Prostriata—a visual area off the beaten path. *Curr. Biol.* **22**, R571–R573 (2012). doi: [10.1016/j.cub.2012.05.030](https://doi.org/10.1016/j.cub.2012.05.030); pmid: [22835792](https://pubmed.ncbi.nlm.nih.gov/22835792/)
76. H. Tamura, K. Tanaka, Visual response properties of cells in the ventral and dorsal parts of the macaque inferotemporal cortex. *Cereb. Cortex* **11**, 384–399 (2001). doi: [10.1093/cercor/11.5.384](https://doi.org/10.1093/cercor/11.5.384); pmid: [11313291](https://pubmed.ncbi.nlm.nih.gov/11313291/)
77. T. Dalmay, L. Ewig, B. Roska, R. Azeredo da Silveira, bioRxiv 2025.02.11.637650 [Preprint] (2025); <https://doi.org/10.1101/2025.02.11.637650>.
78. S. W. Oh *et al.*, A mesoscale connectome of the mouse brain. *Nature* **508**, 207–214 (2014). doi: [10.1038/nature13186](https://doi.org/10.1038/nature13186); pmid: [24695228](https://pubmed.ncbi.nlm.nih.gov/24695228/)
79. Q. Wang, O. Sporns, A. Burkhalter, Network analysis of corticocortical connections reveals ventral and dorsal processing streams in mouse visual cortex. *J. Neurosci.* **32**, 4386–4399 (2012). doi: [10.1523/JNEUROSCI.6063-11.2012](https://doi.org/10.1523/JNEUROSCI.6063-11.2012); pmid: [22457489](https://pubmed.ncbi.nlm.nih.gov/22457489/)
80. R. D. D'Souza *et al.*, Hierarchical and nonhierarchical features of the mouse visual cortical network. *Nat. Commun.* **13**, 503 (2022). doi: [10.1038/s41467-022-28035-y](https://doi.org/10.1038/s41467-022-28035-y); pmid: [35082302](https://pubmed.ncbi.nlm.nih.gov/35082302/)
81. V. Willenbockel *et al.*, Controlling low-level image properties: The SHINE toolbox. *Behav. Res. Methods* **42**, 671–684 (2010). doi: [10.3758/BRM.42.3.671](https://doi.org/10.3758/BRM.42.3.671); pmid: [20805589](https://pubmed.ncbi.nlm.nih.gov/20805589/)
82. A. Syeda *et al.*, Facemap: A framework for modeling neural activity based on orofacial tracking. *Nat. Neurosci.* **27**, 187–195 (2024). doi: [10.1038/s41593-023-01490-6](https://doi.org/10.1038/s41593-023-01490-6); pmid: [37985801](https://pubmed.ncbi.nlm.nih.gov/37985801/)
83. L. McInnes, J. Healy, J. Melville, UMAP: Uniform manifold approximation and projection for dimension reduction. [arXiv:1802.03426](https://arxiv.org/abs/1802.03426) [stat.ML] (2020).
84. P. Morel, Gram: Grammar of graphics plotting in Matlab. *J. Open Source Softw.* **3**, 568 (2018). doi: [10.21105/joss.00568](https://doi.org/10.21105/joss.00568)
85. D. Siegenthaler *et al.*, Visual objects refine head direction coding. *Dryad* (2025); <https://doi.org/10.5061/dryad.2rbnz81t>.

ACKNOWLEDGMENTS

We thank L. Mainville for performing histology for post hoc identification of electrode tracks. We thank T. Frank, A. Krishnaswamy, J.-M. Martinez de Paz, P. Wanken, T. Gollisch, P. Goltstein,

and N. Gogolla for helpful discussions and feedback on the manuscript. We thank G. Montaldo and A. Urban for technical support with fUS data acquisition. We thank K. Asumbisa for help designing the system for head-fixing mice with chronic electrode implants. We thank J. Kuhl for help with figure illustrations. **Funding:** D.S. was supported by the Swiss National Science Foundation (SNSF) Early Postdoc.Mobility nos. 194957 and 211087, and Deutsche Forschungsgemeinschaft Walter-Benjamin Programm (Stelle) no. SI 2831/1-1. E.M. was funded by the Max Planck Society, the Else Kröner Fresenius Foundation through the Else Kröner Fresenius Center for Optogenetic Therapies, the Niedersächsisches Ministerium für Wissenschaft und Kultur through zukunft.niedersachsen, and the Deutsche Forschungsgemeinschaft under Germany's Excellence Strategy - EXC 2067/1- 390729940. We acknowledge funding from the Vanier Canadian Graduate Scholarship to S.S.C.; Canada Research Chairs to A.P. and S.T.; Canadian Institutes of Health Research Project Grants (190289 and 180330) and National Sciences and Engineering Research Council Discovery Grant (RGPIN-2018-04600) to A.P.; and an Alfred P. Sloan Foundation Research Fellowship, Human Frontiers Science Program Career Development Award, Office of Naval Research Global Grant, and Canadian Institutes of Health Research Project Grant (185933) to S.T. We acknowledge funding from a Vision Science Research Network National and International Networking Grant to S.T. and E.M. **Author contributions:** Experiments were designed by D.S., S.T., and E.M. fUS experiments were performed by D.S. Anesthetized electrophysiological experiments were performed by D.S. and J.L.M. Awake electrophysiological experiments were performed by H.D. and S.S.C. Data were analyzed by D.S. SNN modeling work was performed by D.L. The manuscript was written by D.S., A.P., S.T., and E.M. **Competing interests:** The authors have no competing interests to report. **Data and materials availability:** All data and code necessary to reproduce the findings of this paper are deposited at Dryad ([85](https://doi.org/10.5061/dryad.2rbnz81t)). **License information:** Copyright © 2025 the authors, some rights reserved; exclusive licensee American Association for the Advancement of Science. No claim to original US government works. <https://www.science.org/about/science-licenses-journal-article-reuse>. This research was funded in whole or in part by the Swiss National Science Foundation (Early Postdoc. Mobility nos. 194957 and 211087) and Deutsche Forschungsgemeinschaft (SI 2831/1-1 and EXC 2067/1- 390729940); as required the author will make the Author Accepted Manuscript (AAM) version available under a CC BY public copyright license.

SUPPLEMENTARY MATERIALS

[science.org/doi/10.1126/science.adu9828](https://doi.org/10.1126/science.adu9828)

Figs. S1 to S13; Tables S1 to S7; References ([86–102](#)); MDAR Reproducibility Checklist

Submitted 29 November 2024; resubmitted 28 April 2025; accepted 19 June 2025

[10.1126/science.adu9828](https://doi.org/10.1126/science.adu9828)